This is to certify that the

thesis entitled

A Preliminary Study of Hot Corrosion by Sodium Chloride on

A Titanium-Aluminum-Chromium-Niobium Alloy

presented by

Gregary Thomas Dowling

has been accepted towards fulfillment
of the requirements for

Master's degree in Materials Science

Thomas R Bieler

Major professor

Date 7 May 1999

A PRELIMINARY STUDY OF HOT CORROSION BY SODIUM CHLORIDE ON A TITANIUM-ALUMINUM-CHROMIUM-NIOBIUM ALLOY

By

Gregary Thomas Dowling

A THESIS

Submitted to
Michigan State University
In partial fulfillment of the requirements
For the degree of

MASTER OF SCIENCE

Department of Materials Science and Mechanics

1999

ABSTRACT

A PRELIMINARY STUDY OF HOT CORROSION BY SODIUM CHLORIDE ON A TITANIUM-ALUMINUM-CHROMIUM-NIOBIUM ALLOY

By

Gregary Thomas Dowling

In an effort to examine the potential of salt to damage a TiAl alloy (nominal composition in at%, Ti-48Al-2Cr-2Nb), in conditions relevant to heat engines, the alloy was subjected to hot corrosion by application of simulated sea salt by aqueous means. Bare ground specimens were sprayed with seawater solution, dried, and exposed in an air furnace at 760°C for times between 0.1 and 20 ks. Obvious attack occurred in as little as 0.3ks in regions where salt was deposited. In such regions, oxide growth was accelerated and non-adhesive. Regions below accelerated growth were pitted heterogeneously in a manner that indicated the alpha-2 phase was preferentially attacked, particularly in lamellar regions. Mechanical strength was measured by four-point bending testing. A reduction of fracture strength was observed only for specimens with the longest exposure. Pre-oxidized specimens were exposed to a salt fog and then a heat cycle. Accelerated oxide growth was observed after numerous salt application and heat cycles for short pre-oxidation times (3.6 ks) but not for longer pre-oxidation times (360 ks). Intermittent weight gain was measured for short pre-oxidation times (3.6 ks). EDS was used to analyze elemental concentrations on surfaces of all specimens. DTA analysis of salt/TiAl mixtures in N_2 indicate that endothermic reactions occur around 700°C. X-ray diffraction was used to determine the products of the above reactions.

To My Wife

Deborah

ACKNOWLEDGEMENTS

I would like to thank my wife, Deborah, and the rest of my family members for their love and support. I would also like to thank my advisor, Dr. T.R. Bieler, and my committee members, Dr. M. J. Crimp and Dr. J. Lucas, for advice and editorial comments, and Dr. R. Schalek for ESEM work.

This study was partially supported by Air Force Office of Scientific Research PRET Program F49620-95-1-0359.

Table of Contents

List of Tables

List of Figures

CHAPTER 1

INTRODUCTION

Titanium-aluminides are candidate materials for high temperature engine applications. These alloys possess low density, high melting temperatures, good elevated temperature strength and modulus retention, environmental resistance, and good creep properties [1-4].

High temperature components suitable for titanium aluminides are jet engine turbine blades [5, 6], turbocharger turbine components [7], pistons and valves [8]. The proposed operating temperature range for jet engine components using titanium aluminides is from 600°C to 900°C (possibly higher). Turbocharger components are expected to operate at temperatures of 600°C to 700°C for diesel engines, and 850°C and above for gasoline engines [7]. Titanium aluminides proposed for use in these applications range in composition from Ti-23 - 24at% Al and Ti-46 - 52at% Al (Ti_3Al - α_2 phase and TiAl - γ phase including alloys with combinations of these two phases). Composites utilizing silicon carbide (SiC) or alumina (Al_2O_3) fibers in a titanium aluminide matrix [9] have also been considered for the above applications.

Titanium aluminides' resistance to oxidation and hot corrosion has limited their use at high temperature, and their very low ductility at room temperature and fracture toughness is also a concern. Oxidation resistance of these alloys increases as the percentage of aluminum in the alloy is increased [51] and is influenced by additional elements [10]. Oxidation of titanium aluminides in pure oxygen leads to formation of a continuous alumina (γ-Al_2O_3) scale which provides protection to about 1000°C, whereas

oxidation in air leads to formation of a scale consisting of alumina and titania (rutile – TiO_2) and limits protection to about 800°C [33].

There has been very little study about hot corrosion of titanium aluminides. Hot corrosion of metal alloys is defined as the phenomenon of accelerated high-temperature oxidation in a gaseous atmosphere of a material whose surface is coated with a thin film of fused salt. Early studies of this phenomenon were performed to examine the accelerated corrosion of metals in aircraft gas turbine engines. This corrosion was caused by a thin layer of sodium sulfate (Na_2SO_4) that form on the airfoil material from a reaction between sulfur in the fuel and NaCl (ingested during combustion in the form of seawater aerosol) [11]. Sodium chloride can also act directly with engine components when condensation of seawater spray (or mist) lands on engine components while engines are not running at airports near seacoasts. Studies [45,46] have shown that hot corrosion of nickel-based superalloys induces accelerated oxidation and can cause catastrophic oxidation. However, coating nickel-based superalloys with a layer that forms a protective oxide increases the creep rate, reduced rupture life and rupture ductility [33, 39, 41].

Since titanium aluminides are targeted for internal and external applications in turbine engines, hot corrosion should be a concern. Titanium and titanium alloys can be pitted and experience stress corrosion cracking (SCC) when exposed to environments containing chloride salts. Handling and cleaning of parts can also lead to cracking caused by hot corrosion due to salt residues left from fingerprints and chlorinated cleaning solutions [13]. Yao and Merek [15] observed increased weight gain, pitting and grain boundary attack after subjecting a TiAl-based alloy to hot corrosion by NaCl.

This study will be concerned with hot corrosion by NaCl on the alloy Ti-48Al-2Cr-2Nb. Since little research to date has focused on hot corrosion as it applies to titanium aluminides, and for the sake of academic convenience, the research path followed had many short branches which had to be evaluated and assessed as neatly as possible. The study examined many exploratory routes that have provided guidance for further research on the hot corrosion. The need to investigate hot corrosion reactions and their products required use of several analytical tools (i.e., EDS, XRD, DTA, etc.).

The motivation used to provide a focus for this study was to consider the scenario of short inter-island flights having limited duration where salt water vapor has an opportunity to condense on engine parts during down time. From this scenario, exposure times were derived and used in the experimental procedure which includes: analysis of changes in oxide growth, determining if hot corrosion affected the alloy's strength, and investigating if a pre-oxidation layer is protective.

CHAPTER 2

REVIEW OF RELATED LITERATURE

2.1 GENERAL CHARACTERISTICS OF TITANIUM ALUMINIDES

2.1.1 General Aspects of Aluminides

Aluminides are important classes of alloys that have gained much attention because of their unique properties. They possess excellent elevated temperature strength, resistance to oxidation and corrosion, have relatively low densities, and high melting points. These properties result from the fact that aluminides (generally) form ordered intermetallic alloys. The use of most intermetallic alloys are limited by their fracture resistance (although microalloying can enhance it), creep resistance, ambient temperature ductility and fabricability [18]. Some of the most important aluminides are Fe_3Al (DO_3), FeAl (B2), NiAl (B2), Ni_3Al ($L1_2$), TiAl ($L1_0$) and Ti_3Al (DO_{19}).

Iron aluminides, Fe_3Al and FeAl, have excellent oxidation and corrosion resistance when exposed to hostile environments. Their main drawback is low fracture resistance especially in ambient air where embrittlement occurs due to water vapor. However, when tested in an oxygen environment their ductility is quite high. These aluminides also offer low material costs.

The nickel aluminide Ni_3Al possess good oxidation resistance and excellent strength, in fact, it is the most important strengthening constituents in nickel-based supperalloys. Ni_3Al has low fracture resistance due to embrittlement by water vapor. The nickel aluminide NiAl has excellent oxidation resistance at elevated temperatures and has been used as a coating for hot components in hostile environments. NiAl,

however, lacks fracture resistance at ambient temperatures, as well as strength and creep resistance at elevated temperatures.

The titanium aluminides, TiAl and Ti_3Al, have low densities, high retention of strength, and acceptable creep resistance at elevated temperatures. The Ti_3Al alloys have low fracture resistance, structural instabilities, and cracking problems when exposed to hostile environments under cyclic loads. TiAl alloys possess greater strength at elevated temperatures, better oxidation resistance and a lower density than the Ti_3Al alloys.

2.1.2 Characteristics of Ti_3Al Based Alloys

Titanium aluminides based on Ti_3Al have the DO_{19} (Strukturbericht symbol) or *hP*8 (Pearson symbol) crystal structure, which is an ordered hexagonal structure. Ti_3Al is commonly referred to as the alpha-2 phase on the binary TiAl binary phase diagram, Figure 1, and has a wide composition range from 22 at% to 39 at%Al. The most common Ti_3Al-base alloys contain from 8 to 18 at%Nb which improves a majority of mechanical properties; these materials form two phase alloys (alpha-2 + beta/B2). Micro-alloying with Mo, Ta and Cr can provide strengthening, oxidation resistance is enhanced by Mo and Ta, and creep resistance by Mo. The compositions of a few of the more important Ti_3Al-base alloys (from an engineering standpoint) are Ti-24Al-11Nb, Ti-25Al-10Nb-3V-1Mo, Ti-25Al-17Nb, Ti-25Al-17Nb-1Mo and Ti-24.5Al-8Nb-2Ta-2Mo. Table 1 list some important properties of Ti_3Al-base alloys [1]. Ti_3Al has been shown to exhibit limited ductility up to 900°C with an apparent ductile-brittle transition temperature occurring above 600°C. Fracture is entirely by cleavage up to 600°C, above 600°C there are signs of plasticity but the main mode of fracture is still cleavage up to 900°C [2].

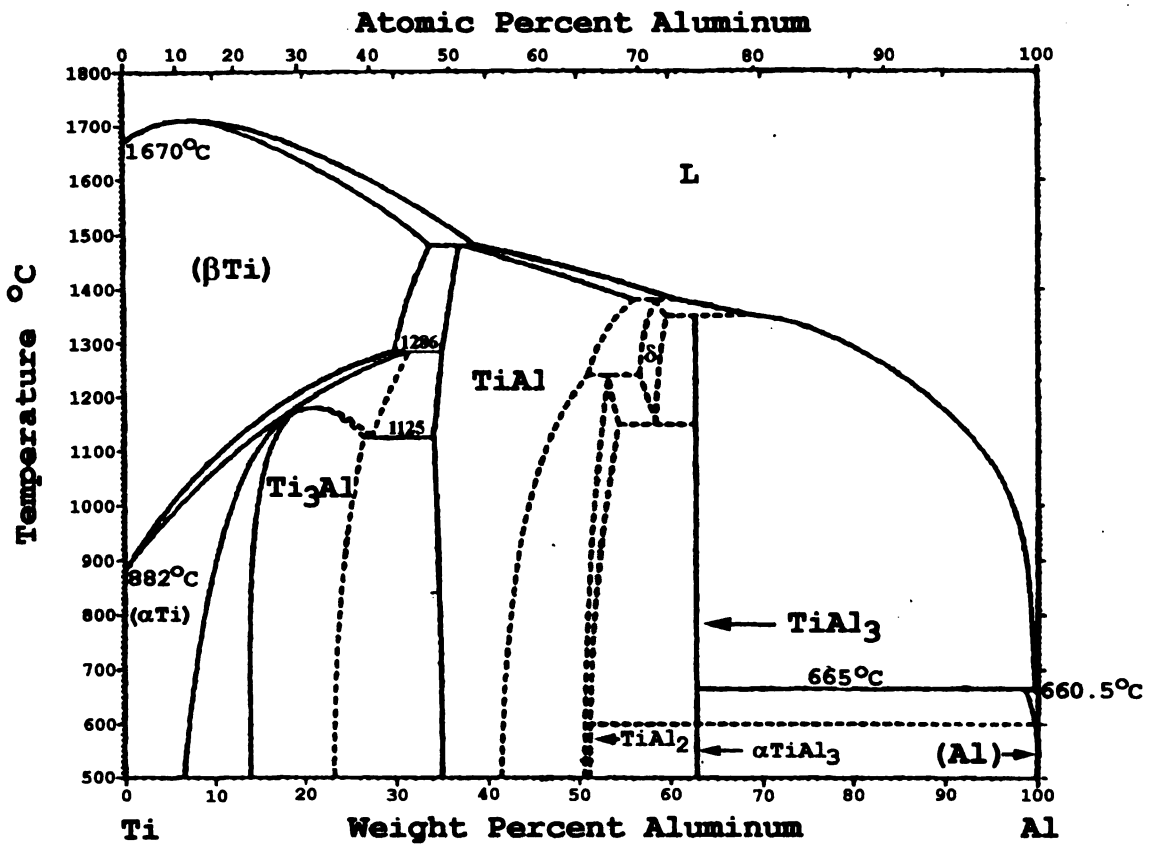

Figure 1. Ti-Al Binary Phase Diagram [19]

Table 1. Selected Properties of Ti_3Al and TiAl alloys [1, 3, 20]

Property	**Ti_3Al-base alloys**	**TiAl-base alloys**
Structure	DO_{19}	$L1_0$
Density (g/cm^3)	4.1 – 4.7	3.7 – 3.9
Modulus (GPa)	110 – 145	160 – 180
Yield Strength (MPa)	700 - 990	400 - 650
Tensile Strength (MPa)	800 – 1140	450 - 800
Ductility (% at RT)	2 - 10	1 – 4
Ductility (% at HT)	10 - 20	10 – 60
Fracture Toughness ($MPam^{1/2}$)	13 – 30	10 - 20
Creep Limit (°C)	760	1000
Thermal Expansion (10^{-6}/°C)	10	12
Oxidation (°C)	650	900

2.1.3 Characteristics of TiAl Based Alloys

Titanium aluminides based on TiAl have the $L1_0$ (Strukturbericht symbol) or $tP4$ (Pearson symbol) crystal structure, which is slightly tetragonal distortion of face centered cubic structure with alternating layers of Ti and Al along the c axis. TiAl is commonly referred to as the gamma phase on the TiAl binary phase diagram, Figure 1, and has a composition range from 44 at% to 52 at% Aluminum. TiAl-based alloys can be divided into single phase (γ) alloys and two-phase ($\gamma + \alpha_2$) alloys. The ($\gamma + \alpha_2$)/ γ phase boundary composition lies at about 49 at.% aluminum at 1000°C and varies depending on the type and amount of other alloying elements added [3]. The single-phase alloys contain from 50 at% to 52 at% aluminum and at least one element such as W, Nb, or Ta [4]. The two-phase alloys contain from 44 at.%-49at.% aluminum and also two or more alloying additions from the group V, Mn, Cr, Nb, Ta, W, Mo, Si, C, B, N, P, Se, Te, Ni, Mo and Fe. Small additions of Nb, Mo, TiB_2 and Ta can improve strength. Oxidation and creep resistance is enhanced by additions of Nb, Si, Mo and W [22], and Cr, V, Mn and Mo can be added to improve ductility.

Several studies [3, 5, 8, 21] have compared the elevated-temperature properties of the single phase (γ) and the two-phase ($\gamma + \alpha_2$) alloys. The lamellar structure of the two-phase ($\gamma + \alpha_2$) alloys gives better ductility and creep resistance than the single phase (γ) alloys. A finer lamellar structure within the duplex microstructure has been shown to increase room temperature ductility. Table 1 list some important properties of TiAl-base alloys [1].

2.1.4 Applications

Titanium aluminides have been studied for use in aerospace, automotive, and power generation applications. Titanium aluminide matrix composites are also being considered for these applications because they have properties which surpass monolithic titanium aluminide [6, 9]

Titanium-based alloys have played an important role in the aerospace industry since the introduction of J57 Turbojet rotors in 1957 [3]. Aerospace research on titanium aluminides has increased due to Government programs. The Integrated High Performance Turbine Engine Technology Initiative (IHPTET) focused on developing TiAl-based engine components. Commercial and military turbine engine manufacturers have proposed using TiAl for turbine engine components [5, 20]. The National Aerospace Plane program (NASP) studied monolithic TiAl-based alloys and/or composites for a high-temperature, lightweight honeycomb or truss core airframe panel structure.

Not only aerospace applications are of interest, but also automotive applications such as turbocharger motors, pistons, and valves stimulate studies on TiAl [8]. These automotive components have been produced from ceramic materials such as Si_3N_4 or SiC, which have lower densities than their metallic counterparts. Low weight is especially important for turbo rotors in that it reduces their inertia and hence minimizes turbo-lag [7]. Superalloys were previously used but their density of about $8g/cm^3$ is much higher than the lightweight ceramics that have a density of about $3.2g/cm^3$. TiAl-based alloys are attractive for this application because they have a density comparable to

ceramics, easier fabrication methods compared to ceramics, and better fracture toughness than ceramics.

2.2 GENERAL CORROSION OF METALLIC MATERIALS

2.2.1 Types of Corrosion

Corrosion can be classified as wet or dry. Wet corrosion involves a liquid, i.e., aqueous solutions or electrolytes. Dry corrosion occurs without the presence of a liquid and usually at high temperatures (above the dew point of the environment). An example of wet corrosion is corrosion of steel by water and an example of dry corrosion is the oxidation of titanium at 500 °C.

The forms that corrosion manifests itself are important for detection and prevention. There are eight forms of corrosion which may be unique to a certain situation but they are related to one another; these are: (1) uniform or general attack; (2) galvanic, or two metal corrosion; (3) crevice corrosion; (4) pitting; (5) intergranular; (6) selective leaching, or parting; (7) erosion corrosion; (8) stress corrosion [23].

2.2.2 Environmentally Assisted Corrosion

Environmental factors such as temperature, concentration and velocity of the corrosive medium can cause and/or accelerate corrosion. The purity of a metal (or alloy composition) will also affect its corrosion resistance. Surface texture (distribution of grain orientations), grain size and the presence (or lack) of inclusions can influence corrosion resistance of metals and alloys. Marine environments are especially corrosive to metallic materials; this is a major concern since about 3/4 of the earth's surface is covered by oceans.

To illustrate the effect of metal purity, consider a nickel aluminide [26] when exposed to solutions of 0.5M NaOH (pH 13.1), 0.5M NaCl (pH 6.5), 0.5M H_2SO_4 (pH 0.7) and HNO_3 (pH 0.6) it had electrochemical behavior similar to nickel which means nickel aluminide could be substituted for nickel and that purity has little affect in those environments.

Another example of purity involves a stainless steel pipe used in cooling systems utilizing seawater. Steel (or iron) will experience pitting and crevice corrosion due to chlorine (from seawater and hypochlorite added to prevent bio-fouling) and operating temperatures of the system. An ELI (extra low interstitial) superferritic stainless steel containing large amounts of Mo and Cr along with small percentages of Ni and Ti will provides excellent corrosion resistance at temperatures greater than 50°C and good repassivation up to 50°C [24].

As mentioned above, a materials texture can influence its corrosion resistance. A study by Gregory and Brokmeier [25] shows that the stress corrosion cracking (SCC) sensitivity is qualitatively dependent on the loading direction and crystallographic orientation. This study was performed on a Ti-6Al-4V alloy in aqueous NaCl solution, and in the presence of a crack.

Variable concentrations (differing pH levels) of the corrosive environment may alter corrosion resistance also. Given three different solutions of 3.5% NaCl with pH's of 3, 7 and 10, polarization tests on Ti_3Al and Fe_3Al show that the breakdown potential is independent of pH but the corrosion potential becomes more positive with lower pH [27].

2.2.3 Mechanical Effect

Mechanical properties such as ductility, fracture strength, yield strength and toughness can be diminished due to exposure to corrosive environments.

In certain cases the stress and the environment are favorable for hydrogen embrittlement (HE) to occur. This is especially true for some aluminides. The ductility was reduced and the fracture mode changed from ductile transgranular to brittle intergranular during SSC testing of a Ni_3Al where HE occurred [28]. Also, Ti_3Al was very susceptible to HE with a cathodic potential beyond – 1000 mV_{SCE} using the slow strain rate technique (SSRT). This alloy exhibited lower tensile strength, lower ductility, surface cracking during plastic loading with transgranular and branched cracking [27].

High temperature oxidation of TiAl intermetallics can cause embrittlement by dissolved oxygen and presumably a loss of tensile properties. In general, sub-surface (α-case) embrittlement is more of a problem with α_2-Ti_3Al based alloys than with γ-TiAl based alloys. McKee and Huang [42] observed α-case formation on γ-TiAl alloys that were oxidation prone such as Ti-48Al-2Cr, after a 850 °C - 900 °C exposure, and with more resistant alloys such as Ti-48Al-2Cr-2Nb, after a 1000 °C exposure.

2.3 OXIDATION OF TITANIUM ALUMINIDES

2.3.1 General Oxidation of TiAl Alloys

The oxide layer(s) which form during high temperature oxidation of TiAl alloys vary depending on the gaseous environment surrounding the sample. An oxygen environment can produce a continuous, protective alumina layer on a binary TiAl alloy up to 1000°C [29], however, exposure in air at 1000 °C forms a scale consisting of TiO_2 and Al_2O_3.

TiAl alloys that contain a third or fourth alloying addition always form a mixed scale of TiO_2 and Al_2O_3 regardless if oxidized in air or oxygen. The scale formation during exposure to O_2 is the following [10]: at the base metal/scale interface is a layer consisting of TiO_2 and Al_2O_3 with small pores distributed throughout the layer. The outer layer consists mainly of large TiO_2 grains, and the region in-between these layers is rich in Al_2O_3 with large voids. The scale is not considered to be continuous because of its porous nature, but provides a barrier and is considered "protective". In contrast, a specimen exposed to an air environment at an elevated temperature, introduces nitrogen into scale growth. The presence of nitrogen, and temperatures above 800 °C, leads to formation of intermixed TiN and Al_2O_3 on the alloy oxide interface that interferes with the development of the alumina-rich layer [31], this may account for the development of a non-protective oxide layer.

2.3.2 Thermodynamic Considerations

In a two-phase ($\gamma + \alpha_2$) TiAl alloy, the oxygen pressure of Al/Al_2O_3 is several orders of magnitudes below that of Ti/TiO_2 in the $TiAl/TiAl_3$ region, so, Al_2O_3 is more stable. But, moving from the $TiAl/TiAl_3$ (Al-rich) region to the $Ti_3Al/TiAl$ (Ti-rich) region, the oxygen pressures of Al/Al_2O_3 and Ti/TiO_2 increases and decrease, respectively, allowing TiO_2 to be the dominate oxide [32]. To protect TiAl alloys up to temperatures in excess of 1200°C it is necessary to develop a continuous Al_2O_3 oxide layer [33]. The challenge is how to suppress the formation of TiO_2 and allow just the formation of Al_2O_3. Reference to the Ellingham diagram for oxides, Figure 2, shows that $\overline{G}^o$ for the formation of Al_2O_3 is more negative than $\overline{G}^o$ for the formation of TiO_2.

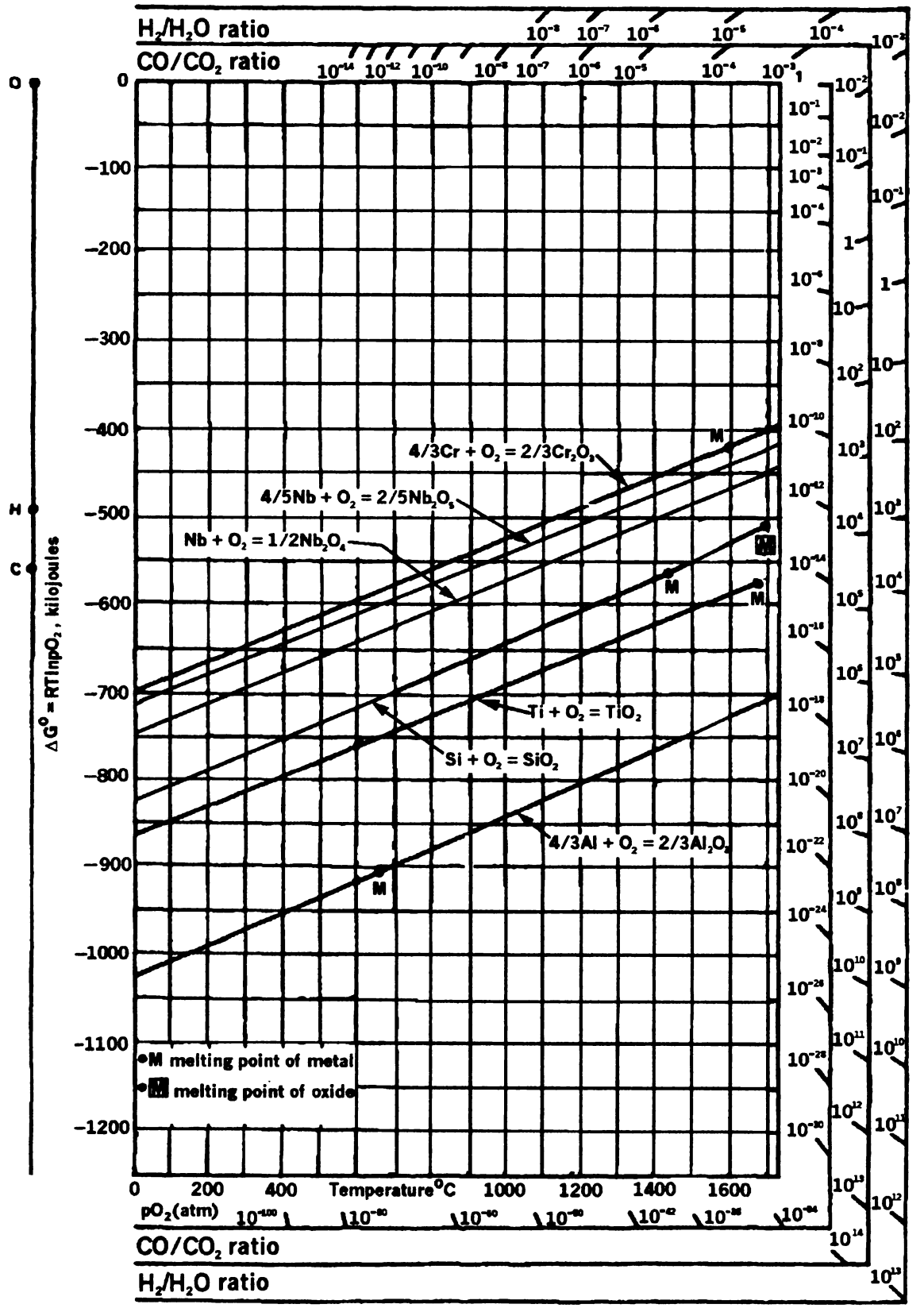

Figure 2. Ellingham Diagram of Some Common Oxides [47].

However, given an expected minimum service temperature of 650° and an oxygen partial pressure of 0.21 atm., it is expected that both oxides will form and in fact they do.

Consider the following reactions taking place during the oxidation of a binary TiAl alloy,

$$2Al_{(l)} + 3/2\ O_{2(g)} = Al_2O_{3(s)} \quad \text{(I)}$$

and

$$Ti_{(s)} + O_{2(g)} = TiO_{2(s)} \quad \text{(II)}$$

The corresponding free energy changes in joules for the above equations are,

$$\overline{G}^{o}_{(I)} = -1676000 + 320T \quad \text{(III)}$$

$$\overline{G}^{o}_{(II)} = -910000 + 173T \quad \text{(IV)}$$

and at 650°C, $\Delta\underline{G}^{o}_{(I)}$ = -1381kJ and $\Delta\underline{G}^{o}_{(II)}$ = -750kJ. Equations (III) and (IV) can be expressed as,

$$\Delta G^{o} = -RTlnK = -RTln[a_{Al2O3} / (a_{Al})^2\ (pO_2)^{3/2}] \quad \text{(V)}$$

and

$$\Delta G^{o} = -RTlnK = -RTln[a_{TiO2} / (a_{Ti})\ (pO_2)] \quad \text{(VI)}$$

Assuming that the activities for Al_2O_3 and TiO_2 are unity and the oxidation occurs in air where pO_2 is 0.21 atm., then equations (V) and (VI) can be rewritten respectively as

$$\Delta G^{o} = -RTln[(a_{Al})^{-2}\ (pO_2)^{-3/2}] = 2RTln(a_{Al}) + 3/2\ RTln(0.21) \quad \text{(VII)}$$

and

$$\Delta G^{o} = -RTln[(a_{Ti})\ (pO_2)]^{-1} = RTln(a_{Ti}) + RTln\ (0/21) \quad \text{(VIII)}$$

By using these equations, the activities of Al and Ti can be found. These activities will change depending on the relative amounts of Al and Ti in the alloy and upon addition of other micro-alloying elements.

Niobium is commonly added to TiAl alloys to enhance oxidation resistance and may form Nb_2O_5 [37] or Nb_2O_4. The reaction to form each niobium oxide and the corresponding free energy expressions are given below.

$$Nb + O_2 = 1/2Nb_2O_4 \quad \text{(IX)}$$

$$\Delta G = -798500 - 20.25T\log T + 243T \text{ J/mol} \quad \text{(X)}$$

$$4/5Nb + O_2 = 2/5Nb_2O_5 \quad \text{(XI)}$$

$$\Delta G = -763600 - 27T\log T + 263.6T \text{ J/mol} \quad \text{(XII)}$$

At 650°C, free energy change to form Nb_2O_4 is –1259kJ/mol and for Nb_2O_5 is -1485kJ/mol.

Thermodynamic calculations between 320 °C and 950 °C show that aluminum and titanium can react with NaCl and oxygen to produce $NaAlO_2$ and Na_2TiO_3, and other products [15]. The following reactions are possible below 800 °C,

$$2NaCl + Al + 4O_4 = 2NaAlO_2 + Cl_2 \quad \text{(XIII)}$$

and

$$4NaCl + Ti + 3O_2 = 2Na_2TiO + 2Cl_2 \quad \text{(XIV)}$$

(the melting point of NaCl is 801°C.) Pertinent thermodynamic data that can be used to find the free energy change for these reactions is listed in Table 2, the last two values are for constant pressure heat capacity in equation form $c_p = a + bT$.

Table 2.Thermodynamic Data for Free Energy Change Calculations [35]

Element or Compound	ΔH_{298} kJ/mol	ΔS_{298} J/(mol)(K)	a	b
NaCl	-411.2	72.13	12.07	
Al		28.29	4.946	2.963
O_2		20.49	7.168	0.998
$NaAlO_2$	-1135	70.71	17.52	
Ti		30.69	5.250	2.520
Na_2TiO_3	-1591	121.7	30.03	
Cl_2			8.760	0.270

The change in free energies for Equations (XIII) and (XIV) can be calculated using the following equation

$$\Delta G = \left[\Delta H_{298} + \int_{298}^{T} \Delta C_p dT\right] - T\left[\Delta S_{298} + \int_{298}^{T} \frac{\Delta C_p}{T} dT\right] \qquad \text{(XV)}$$

Using the same temperature of 650°C (923K) like the above oxidation example, the free energy change for reactions (XIII) and (XIV) at 650°C are –1519kJ/mol and -1782kJ/mol, respectively.

The change in free energy for reactions (I) and (II) at 650°C, $\Delta G_{(I)}$ = -1397kJ/mol and $\Delta G_{(II)}$ = -757kJ/mol. The free energies of formation for Nb_2O_4 , Nb_2O_5, $NaAlO_2$ and Na_2TiO_3 are all lower than those for TiO_2, but close to that for Al_2O_3. Given that Nb is a micro-alloying element in the TiAl alloy and that Na is present in the form of NaCl, from say seawater, all the oxides listed previous can occur if their activities are favorable.

2.3.3 Elemental Influences

The following elements have been found to increase the oxidation resistance of TiAl alloys: Nb, W, Cl, Mo, Si, Zr, Hf, Co, Te, Se and P [10,16,36,37,38]; the first five yield the best results. Micro-additions such as Pd, Pt, Cu, V, Y, Cr and Mn tend to be detrimental to oxidation resistance [10,16,37], whereas Fe, Ni, Co, Au, Ag, Sn, Y, Zr, Hf and Ta have little effect on oxidation resistance [10,16,38].

There are four general rules for selecting an element that might be beneficial to oxidation resistance [10]. The first is the valence-control rule (VCR or the Wagner-Hauffe rule) which involves micro-alloying to slow (or halt) the diffusion of oxygen. Since TiO_2 grows mainly by diffusion of oxygen via oxygen vacancies, reducing oxygen

vacancies in TiO_2 will enhance the growth of Al_2O_3. A study by Schutze and Hald [16] used Cl^- ions to interact with the TiO_2 lattice to reduce the number of oxygen vacancies and thus reduce diffusion rates in TiO_2 limiting its growth.

Wagner's scaling model is another guideline which establishes the criteria to form a protective Al_2O_3 layer on the surface as opposed to forming internal platelets of Al_2O_3 and is given by the following expression,

$$N_{Al} \rangle \left[\frac{\pi g}{3} N_O \frac{D_O V_M}{D_{Al} V_{Ox}} \right]^{0.5} \qquad \text{(XVI)}$$

where N_{Al} is the aluminum content; N_O is oxygen solubility in the substrate; D_{Al} and D_O are diffusivities of aluminum and oxygen in the substrate, respectively; V_M and V_O are volume of TiAl and Al_2O_3 per mole of Al in the alloy, respectively; and g is a conversion factor for the transition from internal to external oxidation. Most of the parameters for TiAl have not yet been established.

A third guideline for selection of elements that will enhance oxidation resistance is choosing an element that will itself form an oxide barrier layer; to date Si, Nb and Mo form such oxides, and these elements have been used in TiAl based alloys. The last guideline involves modifying the initial oxide layer such as occurs with small additions of Zr and Hf. Ion implantation using one of the following has also been investigated: Nb, V, Ta, W, Cr, Al, Y and Ce [10,40]. The implantation of Nb, Ta, W and Al were beneficial to oxidation resistance, whereas, Y, Ce, Cr, and V-implantation were not.

2.3.4 Prevention/Protection

In general, metallic materials can be protected against high-temperature oxidation only by the formation of scales consisting of either Cr_2O_3, Al_2O_3, or SiO_2, because only

these oxides have a sufficiently slow parabolic growth rate [32]. To protect γ-TiAl alloys a continuous Al_2O_3 (α) scale must be formed. However, the engineering alloys that are based on γ-TiAl develop scales that contain mixtures of Al_2O_3 and TiO_2 when oxidized. The problem is even more complex when oxidation occurs in air so that nitrogen reacts with Ti to form a TiN layer close to the metal substrate [33].

Three coating methods have been used to protect γ-TiAl alloys: MCrAlY (M = Ni, Fe and Co), aluminizing, and silicides/ceramics [33]. Aluminizing has been used to protect metals, especially nickel-based alloys for turbine applications [39]. More recently, a fluidized bed of powdered ceramics consisting of mostly Al_2O_3 (60 mass%), and Cr_2O_3, Nb_2O_5 or WO_3 (40 mass%) were used to protect γ-TiAl alloys and Inconel 713C [41]. This process was successful in protecting both types of alloys, and the WO_3 ceramic results gave the best result.

2.4 HOT CORROSION OF MATERIALS

2.4.1 Fundamentals of Hot Corrosion

Hot corrosion is accelerated oxidation that occurs at elevated temperatures caused by salt deposits on metal surfaces. Early studies of this phenomenon were due to failures of boiler tubing and severe attack of gas turbine airfoil materials. Turbine engines were found to have hot corrosion due to Na_2SO_4 (and/or $NaVO_3$), where sodium comes from ingesting seawater aerosol and sulfur (or vanadium) comes from the fossil fuels. Hot corrosion is classified as Type I or Type II [11,43]; Type I describes high temperature hot corrosion (HTHC) in the range of 825°C - 950°C where the condensed salt liquifies (the melting point of Na_2SO_4 is 884°C); Type II or low-temperature hot corrosion (LTHC)

occurs well below the melting point of Na_2SO_4 and is characterized by non-uniform attack such as pitting.

Sodium sulfate (Na_2SO_4) is called an oxyanion-fused salt that exhibits an acid/base chemistry with Na_2O as the basic component and SO_3 the acidic component. This type of salt also acts as an ionic conducting electrolyte. Consequently, hot corrosion is electrochemical in nature, and it involves fluxing of the protective metal oxides as either acidic or basic solutes in the fused salt [43]. Bornstein and DeCrescente [44] performed studies with sulfur coatings and Na_2SO_4 on Ni-Co superalloys and concluded that indeed it was Na_2O which caused hot corrosion to occur and not the sulfur components. This implies that Cl^- ions are not important in hot corrosion conditions.

A model describing the basic electrochemical mechanism that occurs during hot corrosion is shown in Figure 3. A cathodic reduction of SO_3 (as $S_2O_7^{2-}$) or molecular oxygen occurs at different interfaces, the location depends on the availability of ions from the salt and the alloy. Figure 3(a) shows a salt film with a low concentration of transition metal ions and a high permeability of SO_3 or O_2; reduction of the oxidant species takes place at oxide/salt interface, where electrons are supplied directly from the metal oxidation reaction. The oxide/salt interface is then the most basic area within the salt film, and either acidic or basic solutes of the oxide film can be formed there. In the case of Figure 3(b), there is a high concentration and diffusivities of M^{2+} and M^{3+} , and reduction of the oxidant species can occur at the salt/gas interface. This can occur if electron charge is carried through the salt either by the counter diffusion of two differently charged transition metal ions, or as electronic conduction in the film resulting from electrons hopping between the transition metals. The salt/gas interface is then the

most basic area within the salt film, and either acidic or basic solutes of the oxide film can be formed there. Therefore, the reduction reaction governs the gradient in basicity across the salt film and it can be applied to corrosion of multi-component alloys by various salts [11]. The dissolution of the oxide layer and precipitated of the oxide within the salt film continues in either case, but the reforming of the oxide layer may or may not occur depending on the permeability of O_2. The author did not mention relative thickness of the oxide or salt film. Since dissolutioned oxide is reprecipitated within the salt film, its relative thickness should increase.

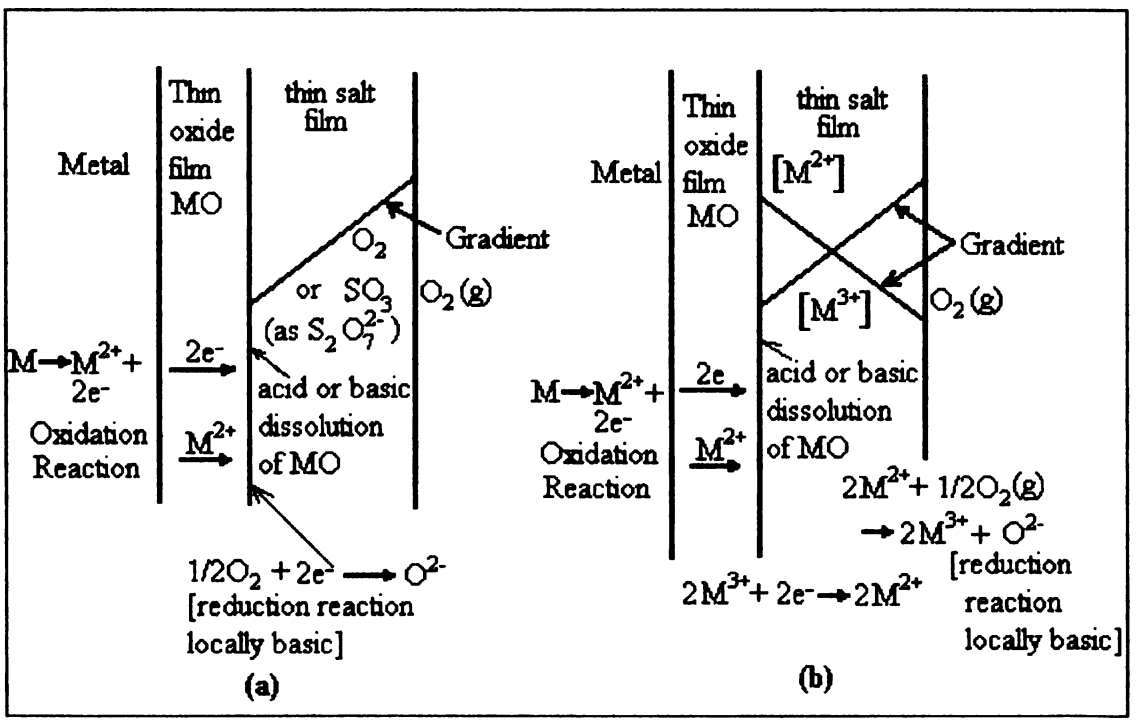

Figure 3. Electrochemical Model [11]

2.4.2 Hot Corrosion of Nickel Based Super Alloys

Hot corrosion (HC) of nickel-base alloys is accelerated oxidation caused mainly by the presence of sodium sulfate (Na_2SO_4), other salts such as sodium metavanadate ($NaVO_3$) and sodium chloride (NaCl) can also cause HC in these alloys.

Nickel-base alloys exhibit two types of HC, either the alloy has oxidation induced by Na_2SO_4 with limited corrosion similar to situations without Na_2SO_4 present or the oxidation induced by Na_2SO_4 is catastrophic. Both Types of HC require a liquid phase present on the surface of the alloy. These reactions need not occur at or above the melting point of Na_2SO_4 (883 °C) since the oxides formed by the alloy combine with Na_2SO_4 to form lower temperature melts.

The hot corrosion of pure nickel and Na_2SO_4 has been studied [45]. Ions within Na_2SO_4 and nickel oxide (NiO) react forming a porous nickel oxide. This reaction is not self-sustaining, it is limited by the amount of Na_2SO_4 present. The activities of the ions to react in the Na_2SO_4 and NiO mix is only favorable during the initial stage of oxidation when conditions are also favorable for the formation of nickel sulfate.

Nickel-based supperalloys can react differently than pure nickel depending on alloying additions. Three common nickel-based alloys, Ni-Al, Ni-Cr and Ni-Cr-Al, were studied for HC by Na_2SO_4 [45]. These were chosen since they develop NiO, Cr_2O_3 and Al_2O_3 as oxides. Observations from the Ni-Al alloys show that Na_2SO_4 accelerates oxidation initially (increased weight gain) and Na_2SO_4 reacted with Al_2O_3 forming $NaAlO_2$, but that the oxidation kinetics were basically unchanged. The Ni-Cr alloys differ from the Ni-Al alloys in that their oxidation weight gain with Na_2SO_4 applied was less than their oxidation weight gain without Na_2SO_4 applied. Also, Ni-Cr alloys have

Cr_2O_3 layer which is protective for an initial time period, and then sulfur from Na_2SO_4 enters the alloy through the oxide layer, sulfur and Cr_2O_3 react forming chromium sulfides below the surface of the Cr_2O_3 scale. The Ni-Cr-Al alloys, with high amounts of Cr, had oxidation weight gains similar to Ni-Cr alloys, whereas the low Cr alloys displayed oxidation weight gains similar to the Ni-Al alloys. The Ni-Cr-Al alloys with high Cr form an initial Cr_2O_3 scale next to the metal interface, then a Al_2O_3 layer starts to form in-between the external Na_2SO_4 deposit and the Cr_2O_3 scale. Sulfur from the Na_2SO_4 diffuses through the porous Al_2O_3 layer and reacts with Cr_2O_3 producing chromium sulfides. After an incubation period, the Al_2O_3 layer becomes continuous and protective stopping further diffusion of sulfur. The Ni-Cr-Al alloys with low Cr do not form a continuous protective Al_2O_3 scale due to sulfur from Na_2SO_4 reacting with Cr at the metal interface, this produces chromium sulfides and preventing the formation of the necessary chromate which is a precursor to continuous alumina formation..

A superalloy containing nickel and cobalt has been studied for HC by sodium sulfate (Na_2SO_4), sodium metavanadate ($NaVO_3$) and sodium chloride (NaCl) [46], this alloy was also subjected to tensile loading during HC. The hot corrosion stress testing using these salts lowers the rupture live of Ni-Co superalloys. However, unstressed specimens have a decreased corrosion rate after time due to the formation of protective nickel vanadates. Consequently, the kinetics of HC differ depending on whether the material is stressed.

2.4.3 Hot Corrosion Due to Sodium Chloride

Hot corrosion due to NaCl on a Ni-Co alloy was mentioned in the above study [46]. The NaCl in the molten salt mixture decreased the solution's viscosity allowing

easier decomposition of Na_2SO_4 which lead to formation of oxychlorides. Several reactions between Ni, NiO, Cr_2O_3, Cr and Cl_2 then result in corrosion at grain boundaries.

Sodium chloride can also cause HC in austenitic and ferritic stainless steels by reactions between Cr_2O_3, Cr and Cl_2 [48]. Hot corrosion resistance in the ferritic steels, can be increased by additions of aluminum, and austenitic steels can be improved by additions of silicon. The author noted that chlorine was detected at grain boundaries while sodium was not, but did not infer that chlorine acts as the corrosion accelerant for these steels. Another study by Fujikawa and Maruyama [49] states that austenitic stainless steels that are exposed to HC by NaCl above 500°C have a greater depth of corrosion. Also additions of Mo are beneficial for corrosion resistance but Cr is only beneficial above the melting point of NaCl (801°C).

A recent study performed by Yao and Marek [15] on a TiAl alloy (Ti-47Al-2Nb-2Mn-7 Vol. % TiB_2) revealed that deposited NaCl accelerates corrosion. They observed weight gain after high temperature exposure, and the NaCl and oxide surface morphology was examined by SEM. In their study, NaCl vapor deposited crystals with an approximate size of 6.5μm x 3μm were uniformly distributed on the specimen (approximately 2.3 x 10^{-4}mg mm^{-2} of NaCl). The specimen was heated in air to a temperature of 760°C (below the 801°C melting point of NaCl) and observed after 0.36ks and 0.72ks. After the first 0.36ks (six minutes) there was nodular growth on and around the salt crystals. After 0.72ks (six minutes later) the growth had accelerated to cover the crystal and a majority of the surrounding area (about twice the crystal's size). These nodules were attributed to formation of Ti and Al oxides. The scale that formed was non-protective.

2.4.4 Laboratory Testing

A salt fog test is an accelerated corrosion test in which specimens are exposed to a fine mist of a solution usually containing sodium chloride but sometimes modified with other chemicals (Ref. ASTM B117) [14]. Burner rigs are also used where the specimen is placed within the exhaust flow which may have a solution of salts injected into the flow. A typical test cycle consists of 3 minutes at 845°C (1550°F), idling; 2 minutes at 1010°C (1850°F), takeoff; then removal from the flame for 2 minutes, engine shutdown [12]. Another test is a Dean test in which Na_2SO_4 is heated to above about 1100°C to establish an appropriate vapor pressure and the sample is maintained at a temperature below the dew point where condensation occurs [50].

Experimenters have used various methods for applying salt to specimens for example: specimens are dipped in a solution of NaCl [49], soaked in NaCl (26%) for 5 min [48], sprayed with a solution of Na_2SO_4 (60 wt%), $NaVO_3$ (30 wt%) and NaCl (10 wt%) onto heated specimens at 150°C [46], coated the specimen with 0.5mg/cm^2 of Na_2SO_4 by spraying the solution on a heated specimens at 150°C [45]. They have also tried different heat cycles; heating for 2 hours at 450-850 °C then air cool [49], heating for 2 hours 450-750 °C then air for cool 5 minutes – repeat for 50 cycle [48], heat for 100 hours at 900 – 975°C then air cool [46].

2.5 STRATEGY FOR INVESTIGATING HOT CORROSION

2.5.1 Hot Corrosion Summary

Hot corrosion (HC) is electrochemical in nature and involves an oxyanion-fused salt that exhibits an acid/base chemistry. The salt sets up a flux of ions which uses a metal's (or alloy's) oxide(s) as an electrolyte.

The hot corrosion of nickel-based superalloys has been studied and well documented. Sodium sulfate (Na_2SO_4) is the salt that has the most corrosion potential for HC of nickel-based superalloys. Sulfur ions diffuse through an alloy's oxide(s) to form either nickel or chromium sulfides. Other salts that are known to cause HC in nickel-based superalloys are sodium metavanadate ($NaVO_3$) and sodium chloride (NaCl).

Stainless steels can experience HC by NaCl, it has been extensively studied for this common material. Chloride ions diffuse through the steel's oxide and react with chromium carbides, this causes pitting and intergranular attack. The chromate oxide, which protects stainless steels, can also be attacked by chloride ions.

Titanium aluminides have had limited HC studies performed on them. Two recent studies focused on the HC of titanium aluminides by NaCl [15] and by a sulfur environment [52]. It was theorized that sodium can react to form compounds with oxygen and aluminum or titanium. Sodium chloride was found to accelerate a porous non-protective oxide growth in air but it has no effect on the alloy in an oxygen-free environment. The HC by a sulfur environment caused the TiAl alloy to develop a non-protective oxide scale that spalled off. The study also determined that sulfide precipitates formed at the interface of the oxide and the metal.

2.5.2 Research Approach

This study will investigate the hot corrosion of the intermetallic TiAl (nominal composition in at% Ti-48Al-2Cr-2Nb) by sodium chloride (NaCl). The scenario used to motivate the investigation is to consider aircraft engines operating in frequent short flights of about 1.8ks (30 min.) in a marine setting such as the Hawaiian Islands.

The NaCl used was a simulated seawater solution (ref. ASTM D 1141–90) deposited by airborne application (atomized in a fog). The method is similar to ASTM B117 [14], which was chosen due to its ease of reproducibility in the laboratory, convenience and expense. Bare ground and pre-oxidized TiAl specimens were coated with a thin layer of salt water in a manner that simulates conditions for engines at rest in coastal airports and similar to conditions experienced in coastal regions [30]. Specimens were heated in an air environment to 760°C for various times, then quickly air-cooled. The times represent start-up and immediate shutdown of an engine; start-up, short flight and then shutdown in repetition. These times were chosen because there is no set duration in the literature for HC testing, so experimenters have more or less developed their own procedures. More developed procedures exist for burner rig testing [12].

The compositions of the surface and subsurface layers were measured using EDS. This was used to determine if sodium or chloride was present (or not present) similar to findings in previous studies [15,46,48,49]. Flexural (four-point bend) testing for strength degradation was performed after the heat cycles along with surface morphology examination by SEM. The method and fixtures used for the bend test are similar to ASTM C 1161 (flexural strength of advanced ceramics at ambient temperatures). This was chosen because of the brittle nature of ordered intermetallic materials. An interrupted weight gain experiment was run to verify accelerated oxide growth, like those previously performed on this alloy [33]. Differential Thermal Analysis (DTA) on powdered metal and simulated sea salt at temperatures from RT to 900°C, and Powder X-ray Diffraction (XRD) was performed to analyze the many possible reactions and reaction products that might occur. Due to the use of different micro-alloying elements in

TiAl alloy, that can alter the activities of the constituents of these alloys, and depending on the exposure environment, many different reactions occur and products result [15, 52].

CHAPTER 3

EXPERIMENTAL PROCEDURE

3.1 MATERIALS

The material used for this study came from an investment cast plate of composition Ti-47.9Al-2Cr-2Nb (PRET material). The plate was cast at Howmet Corp. (Whitehall, MI.) and was heat treated at 1093°C for 5h, hot isostatically pressed (HIPed) at 1205°C for 4h and heat treated at 1205°C for 2 additional hours followed by rapid cooling. Also, a sample of mechanically alloyed TiAl powder was used for part of the differential thermo-analysis testing.

3.1.1 Salt Application, Four-Point Bend and Pre-oxidation Specimens

Specimens utilized for the salt application, four-point bend testing, pre-oxidation study and the weight gain study were cut using electrodischarge machining (EDM). The specimens were ground using a series of SiC grinding papers from 240 to 600 grit to remove the EDM heat affected area (resulting dimensions were approximately 34.0mm x 4.0mm x 1.3mm) and then ultrasonically cleaned in acetone.

3.2 SALT APPLICATION

Several specimens measuring approximately 37.0mm x 7.0mm x 4.3mm had simulated seawater solution (Aquarium Systems Instant Ocean®) of approximately 3.5 % salinity with pH = 9.0 applied by means of a fine mist. Three methods were explored to apply the salt water, using a spray bottle on specimens inclined at an angle of about 60°, or creating a fog using either a nebulizer (OMRON Corp. Air Nebulizer Model NE-C08 CompAir®), or a 1 meter tall standing pipe with an air stream blowing bubbles in salt water at the bottom of the column. One sample was exposed on a residential balcony on the NW

side of Maui, at a distance of about 50 yards from the coast, to determine how salt was deposited in natural conditions. The nebulizer method was finally determined to produce a salt distribution most similar to that occurring by coastal regions (similar to the salt distribution on the Maui exposed specimen). The spray bottle method was used on the first group of specimens, but all subsequent groups of specimens had salt applied by the nebulizer method. The nebulizer was filled with 3 ml of simulated seawater for a run time of about five minutes. The nebulizer output was connected to a 9.5mm inner diameter and 1.5m long coiled polymer hose with a coiled structure, which in turn was connected to a polymer funnel as illustrated in Figure 4. The hose prevented the larger droplets from reaching the specimen, and the funnel directed the flow evenly to the specimens and restricted stray air currents. The specimens were then allowed to air dry for 24 hours. Morphologies of the deposited salt crystals were viewed using a light microscope to measure the size distribution and area of coverage.

3.3 FOUR-POINT BEND

Specimens were heated in a Lindberg furnace in an air environment. The specimens were placed on a layer of alumina powder on a copper plate. A control thermocouple was connected to the copper plate. Groups of specimens were exposed for 0.15 ks, 0.36 ks, 1.08 ks, 4.4 ks and 19.44 ks at 760°C. A control group of specimens, which did not have any salt application, was exposed for times of 0.0 ks, 0.36 ks, 1.08 ks and 19.44 ks at 760°C. The specimens were removed from the furnace and air-cooled on a refractory brick.

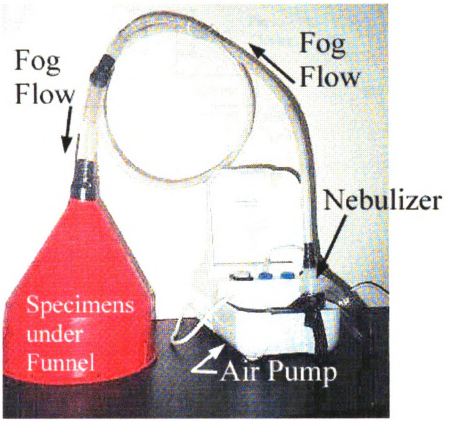

Figure 4. Nebulizer Set-up to Apply Salt Fog to Specimens.

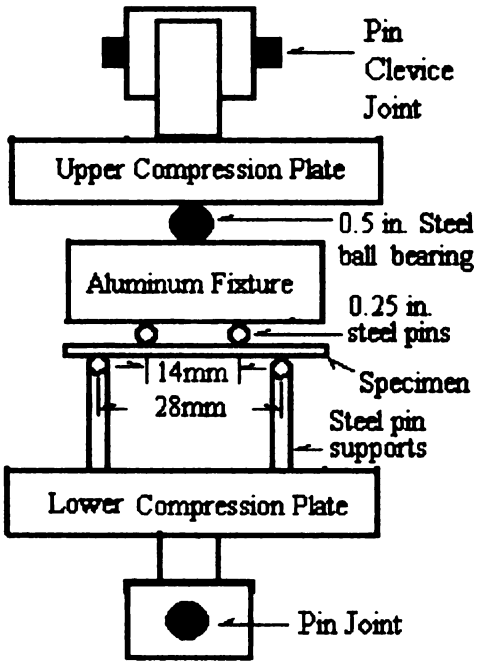

Figure 5. Test Fixture for Four-Point Bending

An environmental scanning electron microscope (ESEM) Electroscan™ model 2020 was used to view and analyze the resulting surface morphology of the heated samples to examine how hot corrosion occurred. The environment within the ESEM was water vapor at a pressure of 2.5 to 5 torr. Energy Dispersion Spectroscopy (EDS) was used to analyze certain areas of interest while viewing the specimens using the ESEM.

After ESEM analysis the specimens were subjected to a four-point bend test. The four-point bend tests were performed using an Instron 4206 tensile/compression tester and the fixture shown in Figure 5. The specimens were loaded by downward movement of the crosshead applied at a rate of 0.1 mm per minute. Morphologies of the fracture surfaces were studied using a JEOL 6400 SEM.

3.4 PRE-OXIDATION

A set of specimens was pre-oxidized in the furnace prior to application of a salt fog and 760°C exposure. Half of the specimens were pre-oxidized for 3.6 ks and the other half for 360ks; all were pre-oxidized in an air environment. Salt was applied to all specimens followed by a 1.08ks, 760°C exposure. The salt application and heat cycle were performed ten times on the 3.6ks specimens. Some specimens had salt applied every cycle while others had salt applied every other cycle. The 360ks specimens were exposed to just a single salt and heat cycle. After each cycle the specimens were viewed using a light microscope and ESEM, and if there seemed to be a change from one cycle to another photos were taken and EDS performed.

3.5 WEIGHT GAIN

Another set of specimens was pre-oxidized in the furnace prior to application of a salt fog and 760°C exposure. These specimens were extra pieces from the casting. The

specimens were ground using a series of SiC grinding papers from 240 to 600 grit to remove the EDM heat affected area and then ultrasonically cleaned in acetone. All specimens were pre-oxidized for 3.6 ks (1 h) in an air environment. After the pre-oxidation, one specimen (specimen S) had salt applied to all of its surface area, two specimens (specimens H1 and H2) had salt applied to half of their surface area and the other half of their surface area was masked using a Kimwipes® paper tissue to prevent salt from reaching the surface, and one specimen (specimen NS) was used as a control that had no salt applied to its surface area at all. The surface areas were approximately 6.10cm^2 for specimens S and NS, and 4.84cm^2 for specimens H1 and H2. Specimens were run through ten cycles of salt application and heat exposure, except for the control specimen that was only exposed to the heat cycle. Initially and after each cycle the weight of each specimen was taken using a Denver Instrument Co., Model A-200D scale with a sensitivity of +/- 0.0001g and recorded. 35-mm photographs of the resulting surface appearance were also taken.

3.6 DIFFERENTIAL THERMAL ANALYSIS

A piece of the casting from which previous samples were taken was used to obtain a fine powder for Differential Thermal Analysis (DTA). The casting was held in a vice and a steel file was used to obtain filings. After a significant amount of filings were obtain a magnet was used to separate the steel filings from the casting filings. This was accomplished by moving the magnet directly below a thin piece of paper, on which both types of filings were lying. This process was done as many times as possible until it was seen that the magnet attracted no more steel filings.

Two different mixtures of simulated sea salt and casting filings (or the mechanically alloyed TiAl powdered metal) were prepared for DTA testing: one mixture had a weight ratio of 9:1 and the other had a weight ratio of 1:9, simulated sea salt to casting filings, respectively. The amounts for the mixtures were measured using a Denver Instrument Co., Model A-200D scale with a sensitivity of +/- 0.0001g. The constituents for each mixture were mechanically combined using an alumina mortar and pestle for a period of 7 to 10 minutes until the mixture "looked" homogeneous. The mixtures were then placed in a glass vessel and sealed with a polymer lid (creating a reasonably air tight seal.)

DTA runs were performed using TA Instruments 910 Differential Scanning Calorimeter equipped with a 1600 DTA test fixture along with Thermal Analysis 2200 data acquisition system and software. Trials were run with sample sizes of approximately 30 mg from room temperature to 900°C at a ramp rate of 20°C/minute with a 100 ml/minute nitrogen gas purge. The standard used was 99.999% pure aluminum.

3.7 X-RAY DIFFRACTION

Powder samples from the DTA castings were used for X-ray diffraction analysis. The powder was attached to the surface of a 2.5mm X 76mm X 1.5mm soda-lime glass slide using petroleum jelly in a 5mm X 15mm area. A Scintag model XDS 2000 diffractometer and associated software was used. The system was set to scan from 20 to 90 degrees for the 9:1 salt to powder ratio and from 5 to 90 degrees for the 1:9 salt to powder ratio at a scan rate of 0.5 degrees per minute.

CHAPTER 4

RESULTS

4.1 INTRODUCTION

The results obtained from the various experimental methods employed clearly indicates that exposure to salt followed by elevated temperatures will cause hot corrosion of the alloy Ti-48Al-2Cr-2Nb. There is evidence of reactions occurring between bare ground specimens and salt, but pre-oxidation appears to prevent these reactions from happening. Exposure to salt and elevated temperatures for long times (about 20ks) only slightly degrades the fracture strength of this alloy, but the statistical scatter of the data can be attributed to surface or interior microstructural flaws present as suggested from fracture surface micrographs.

4.2 SALT DISTRIBUTION

Salt crystals deposited by means of water vapor were either small singular crystals with a sharp rectangular shape or a cluster of rectangular crystals with a roughly circular shape. The salt particles had a size range from about 1 to 30 microns and covered up to 15% of a specimen's area. The small crystals often formed in grooves from the grinding. The spray bottle method caused a few large water spots, which deposited salt cluster with sizes close to 150 microns. Figure 6 shows the salt particle distribution that occurred due to natural exposure near the seacoast and Figure 7 shows the salt particle distribution that occurred by using the nebulizer method. The naturally exposed specimen had the smallest area coverage, but the size distribution was most similar to the method that used the nebulizer. Figure 8 shows the salt distributions by nebulizer, natural exposure, and 4in.-dia. standing tube (specimen placed two feet above air agitated seawater solution).

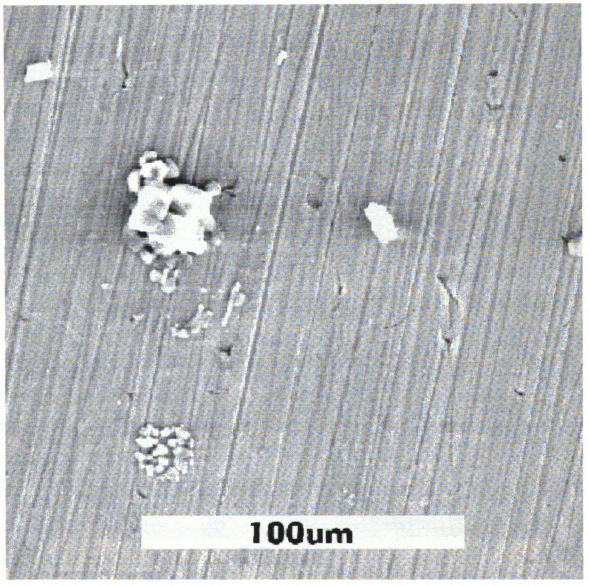

Figure 6. Naturally exposed salt distribution.

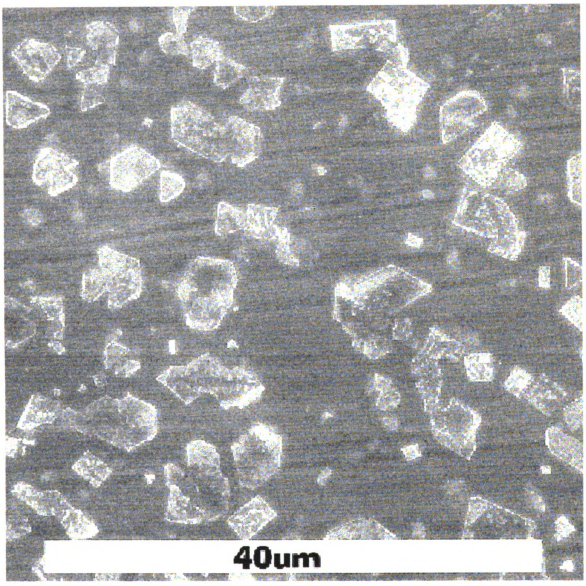

Figure 7. Nebulizer salt distribution.

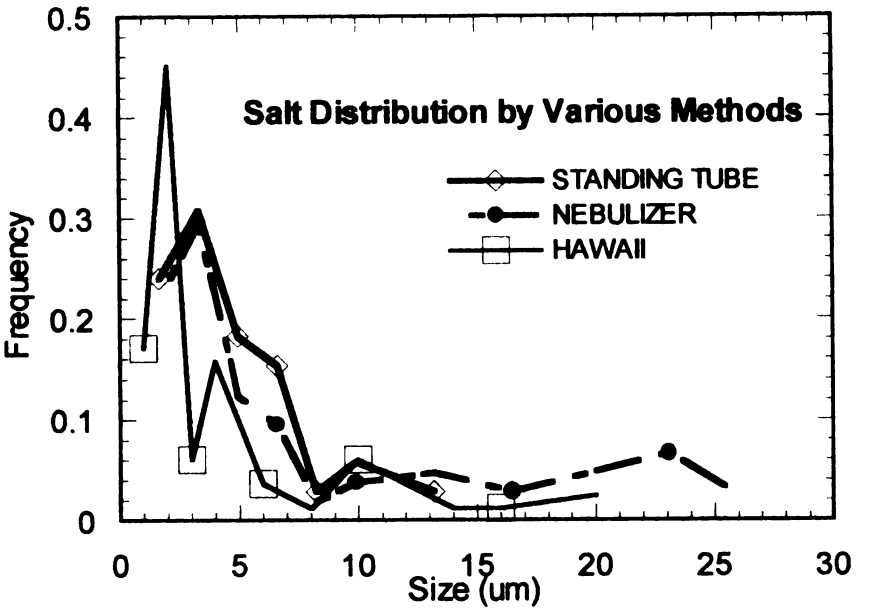

Figure 8. Salt particle size distribution

4.3 SALT ATTACK ON BARE GROUND SPECIMENS

The general features of salt attack were similar for the spray bottle and the nebulizer specimens, (excepting the large clumps of salt on the spray bottle specimen), so images of attack are shown together. An environmental scanning electron microscope (ESEM) along with energy dispersion spectroscopy (EDS) were used to determine if hot corrosion by salt altered the composition, surface and interfacial morphologies of the alloy. A summary of EDS results measured on different features is presented in Figure 9 through Figure 11. The results are displayed as a ratio of the element of interest counts to total titanium counts obtained at a particular area, i.e., all scans are standardized to total titanium counts for that particular scan. EDS was performed on an electropolished specimen, which was not exposed to a heat cycle or salt fog, to obtain a basis for the rest of the measurements taken. This will be referred to as the "base metal" and is indicated on the vertical axis in Figure 9 through Figure 11.

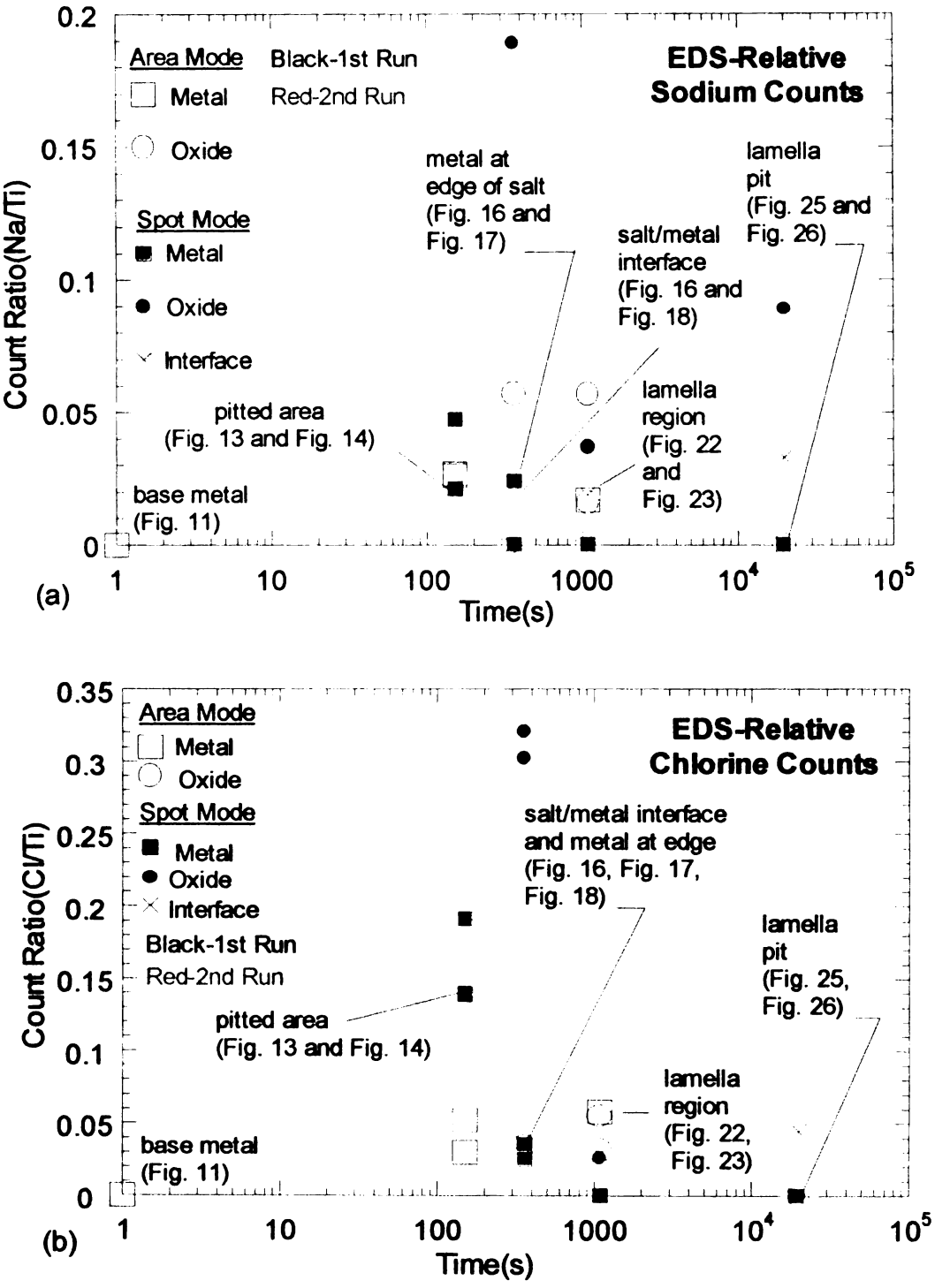

Figure 9. Ratio of EDS intensity for (a) Na, (b) Cl.

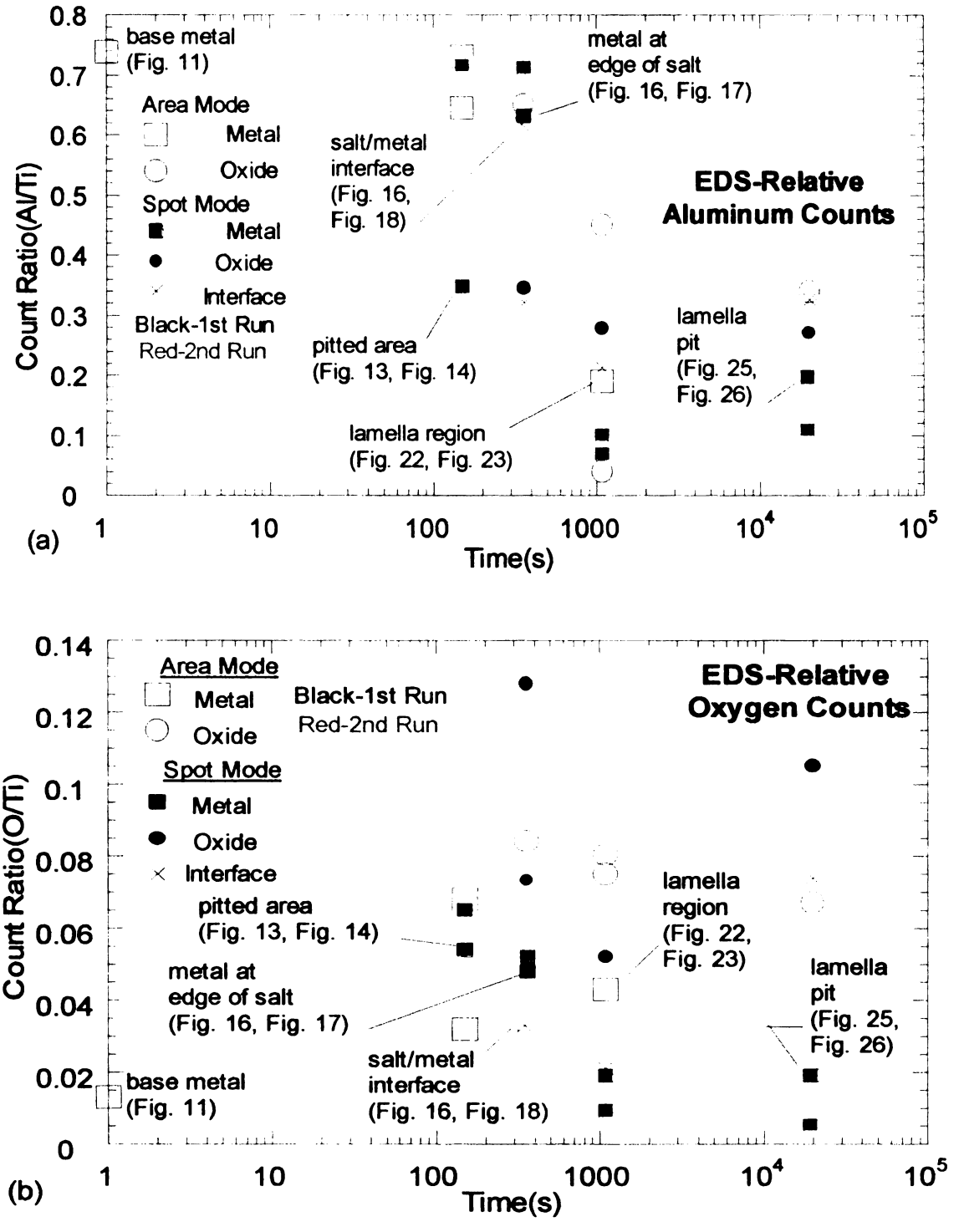

Figure 10. Ratio of EDS intensity for (a) Al, (b) O.

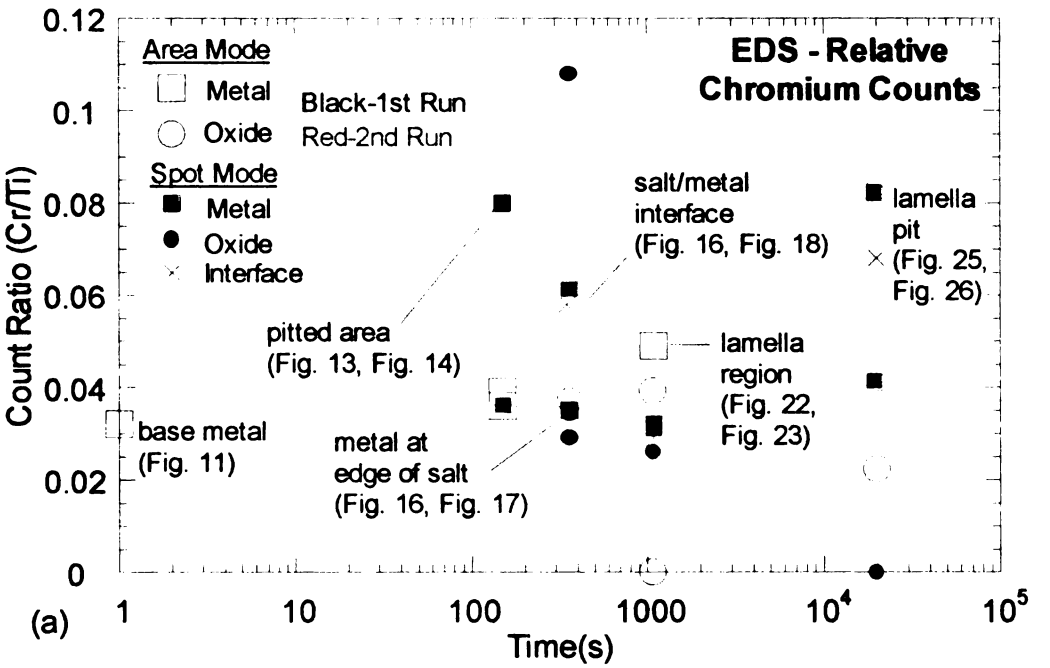

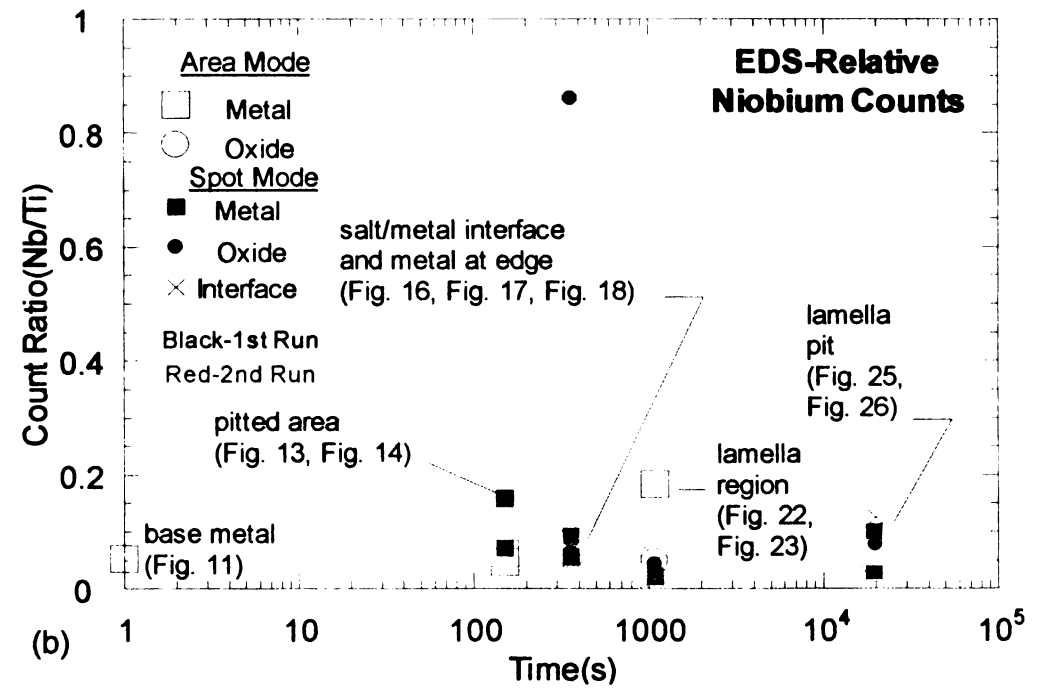

Figure 11. Ratio of EDS intensity for (a) Cr, (b) Nb.

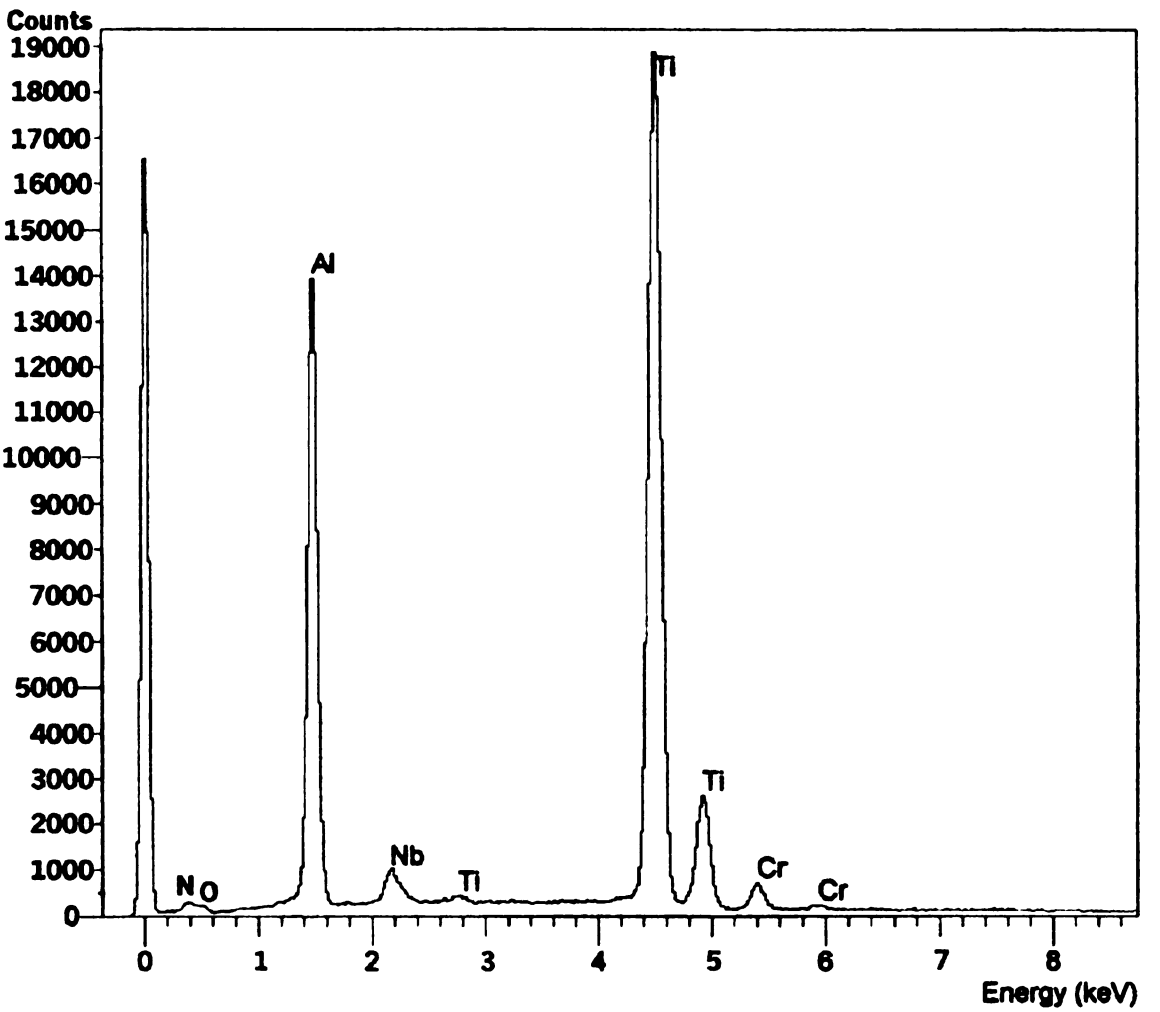

Figure 12. EDS scan of electropolished specimens – "Base Metal".

Images were taken at particular areas of interest are shown in Figure 13 through Figure 26. Sample EDS scans for a few of these areas immediately follow the photograph. The data obtained from the EDS scans was used to create the plots shown in Figure 9 through Figure 11. Figure 12 is the EDS scan of the base metal, the specimen used was electropolished and was stored in an open-air environment (this may account for the detection of nitrogen and oxygen).

Figure 13 and Figure 14 depicts the general surface of the 0.15 ks specimens. Salt crystals have spread out forming tree-like structures indicated by the arrow in Figure 13. EDS reveals small concentrations of Na and Cl in these areas. In another area with a salt clump adjacent to a pit, there are larger Na, Cl and O concentrations, and lower Al, Cr, Nb concentrations compared to the base metal (Figure 14). The EDS scan of this pitted area is shown in Figure 15.

The surface morphologies of the 0.36ks specimens show various stages of oxide growth. Figure 16 shows growth of oxide that follows the tree-like structure seen on the 0.15ks specimens. Four distinct regions can be identified in Figure 17. The topography rises from region 1 where a salt clump chipped off to the thin oxide layer of region 4. Region 1 is where the salt deposit was originally and then got knocked off. Region 2 is the interface region between the salt and the metal (Figure 19 is the EDS scan). The metal is apparent in region 3 (Figure 18 is the EDS scan). A thin oxide layer is identified in region 4. Around the salt particles on these specimens, there is an increase in the Na and Cl concentrations, the O concentration stayed about the same, and there was a decrease in the Al and slight decreases in Nb and Cr concentrations. The obviously attacked areas on the 0.36 ks specimens had a decrease in Al concentration, and increases in the Cr, Cl and

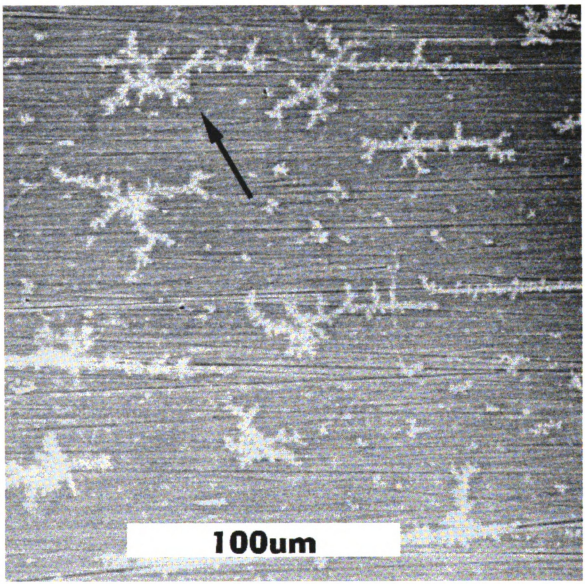

Figure 13. 0.15ks specimen - general area.

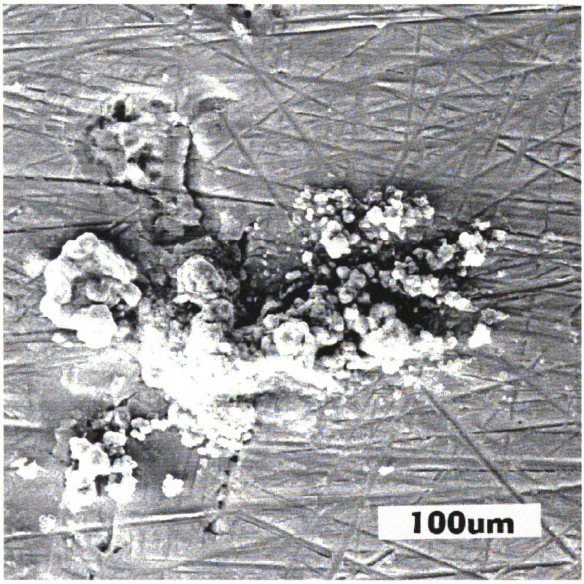

Figure 14. 0.15ks specimen - salt clump near a pit.

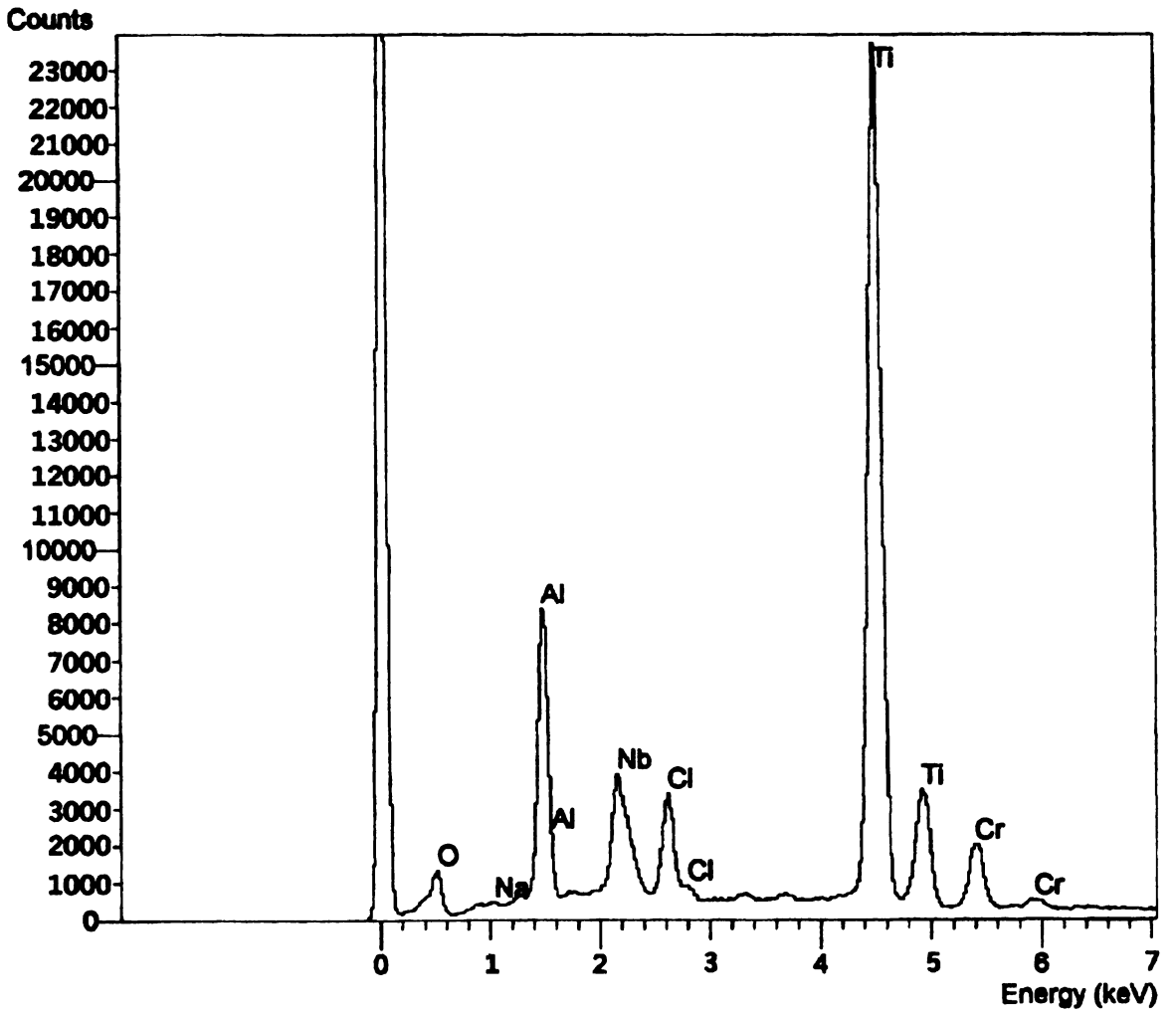

Figure 15. EDS scan of a surface pit on 0.15ks specimen (Figure 14).

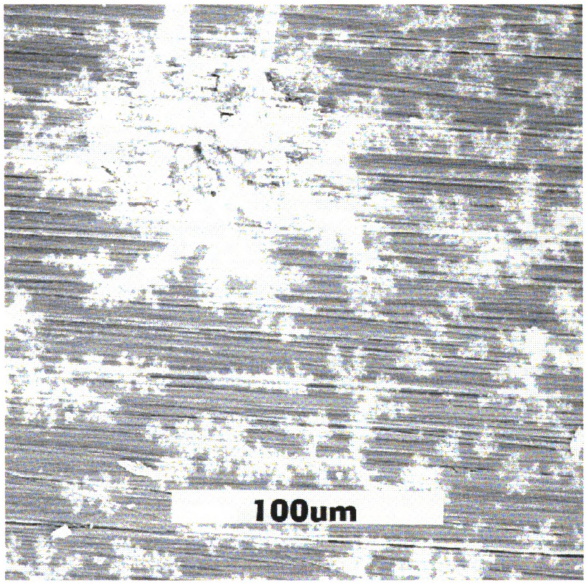

Figure 16. 0.36ks specimen - accelerated oxide growth.

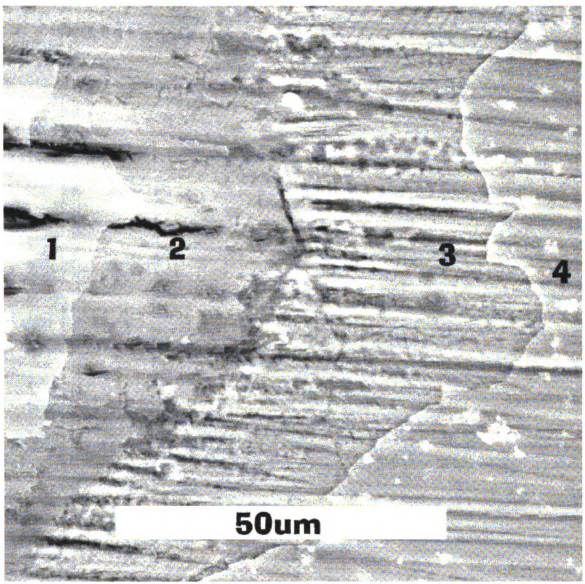

Figure 17. 0.36ks specimen – exfoliated salt deposit.

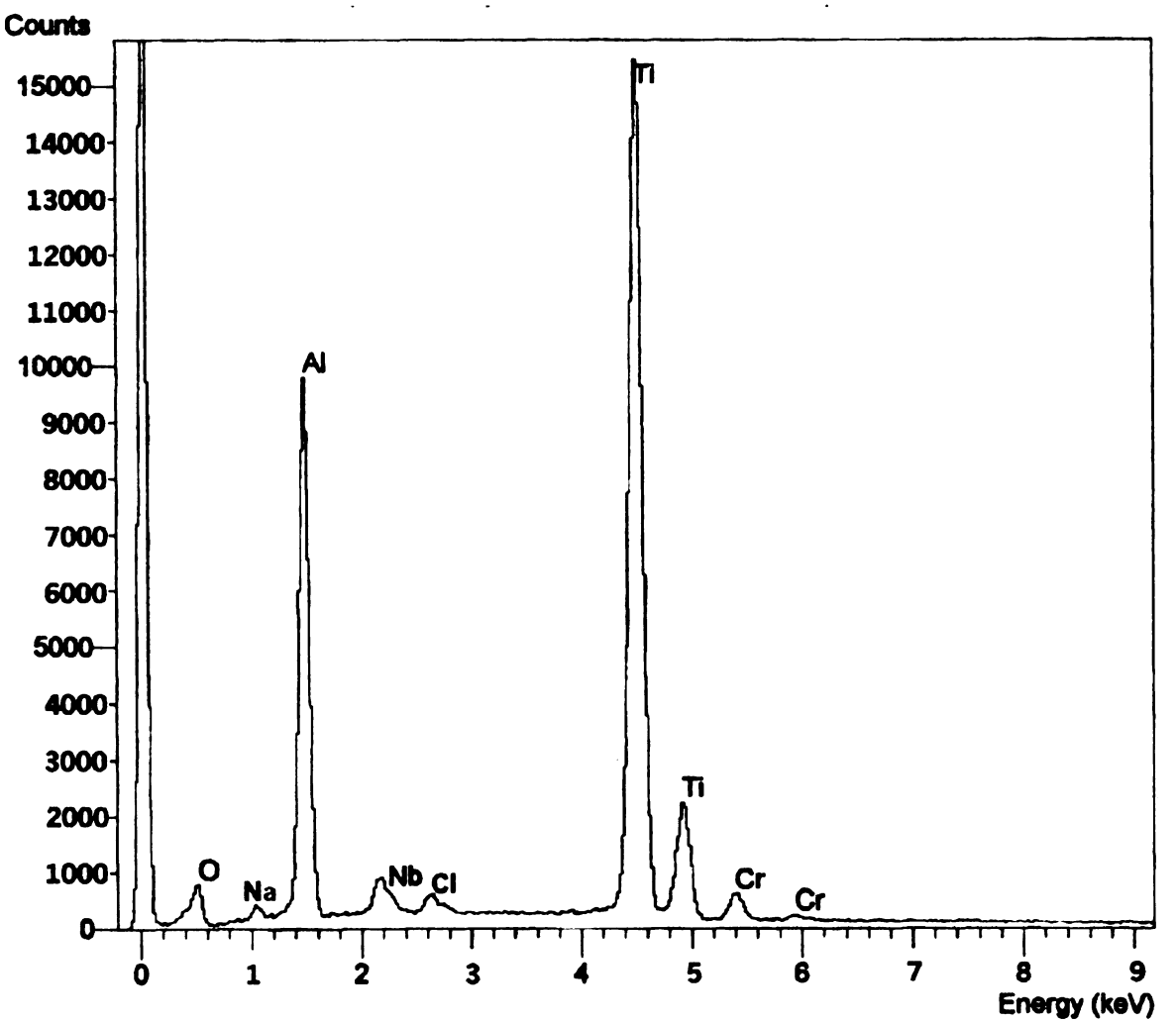

Figure 18. EDS scan of the metal at edge of exfoliated salt deposit (region 3).

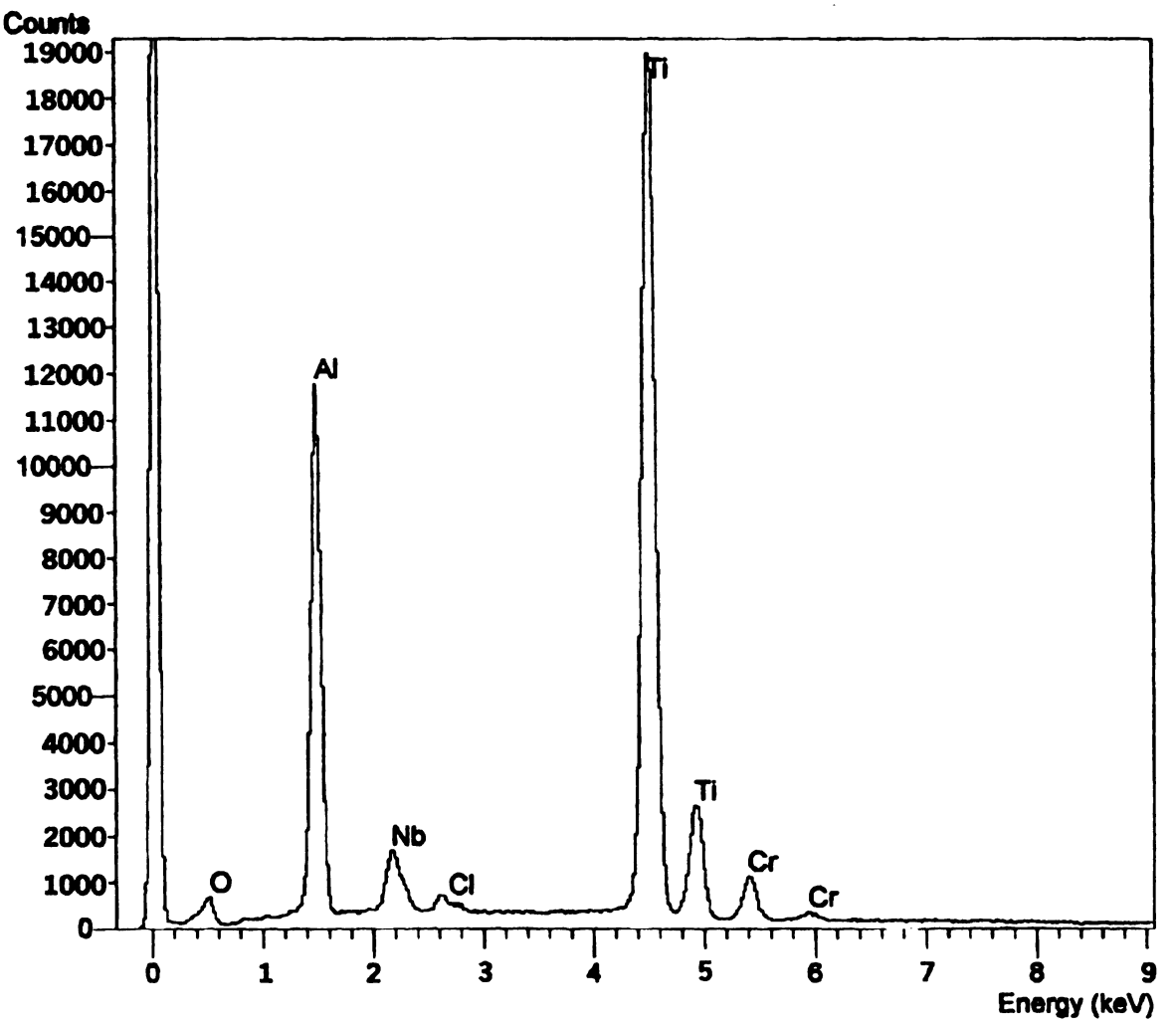

Figure 19. EDS scan of the metal/salt interface by exfoliated salt deposit (region 2).

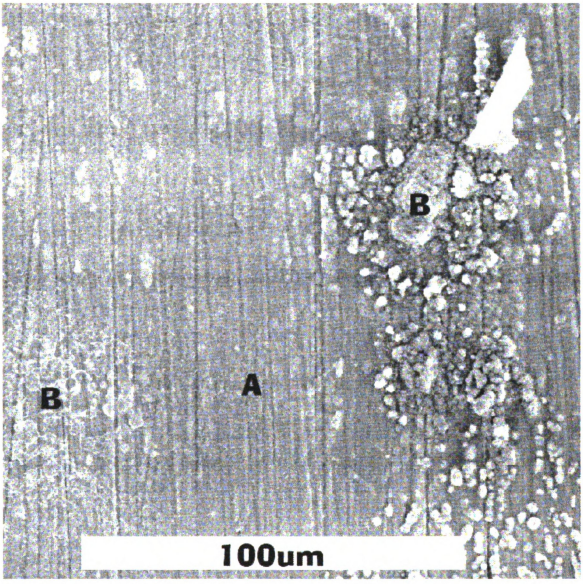

Figure 20. 0.36ks specimen - light and heavy salt deposits and resulting oxide.

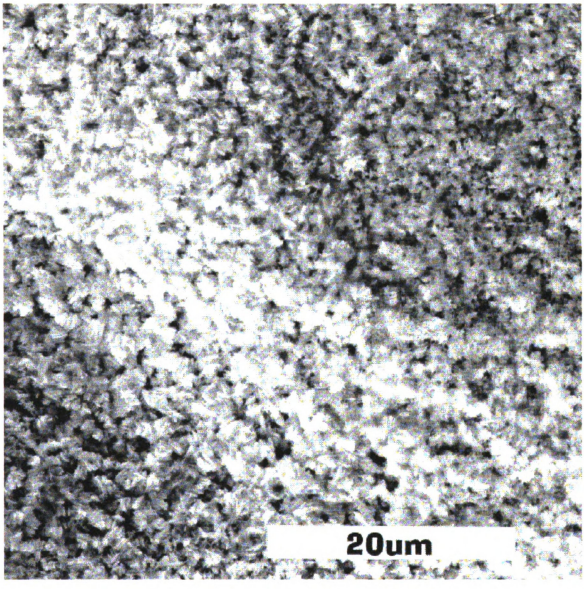

Figure 21. Surface morphology of specimen exposed for 1.08ks - general oxide.

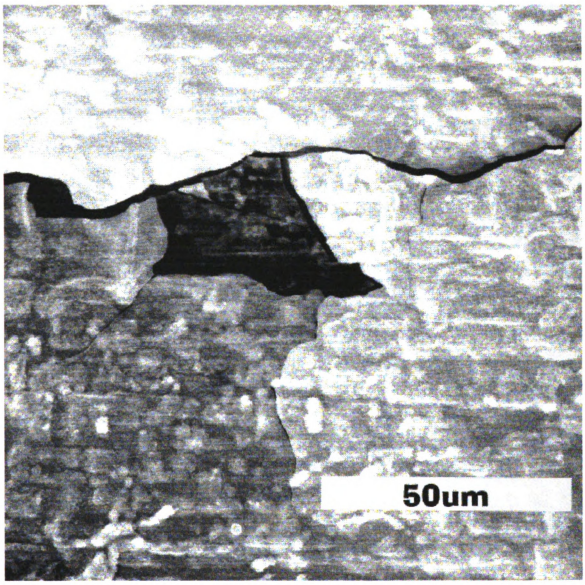

Figure 22. Surface morphology of specimen exposed for 1.08ks - fracture in oxide.

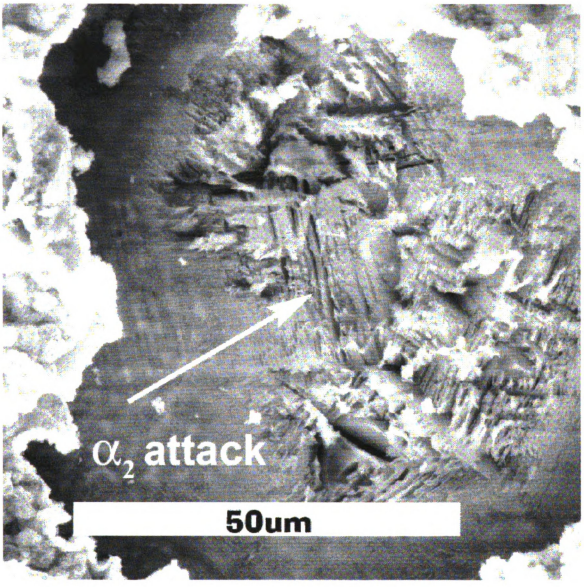

Figure 23. Surface morphology of specimen exposed for 1.08ks - damaged area.

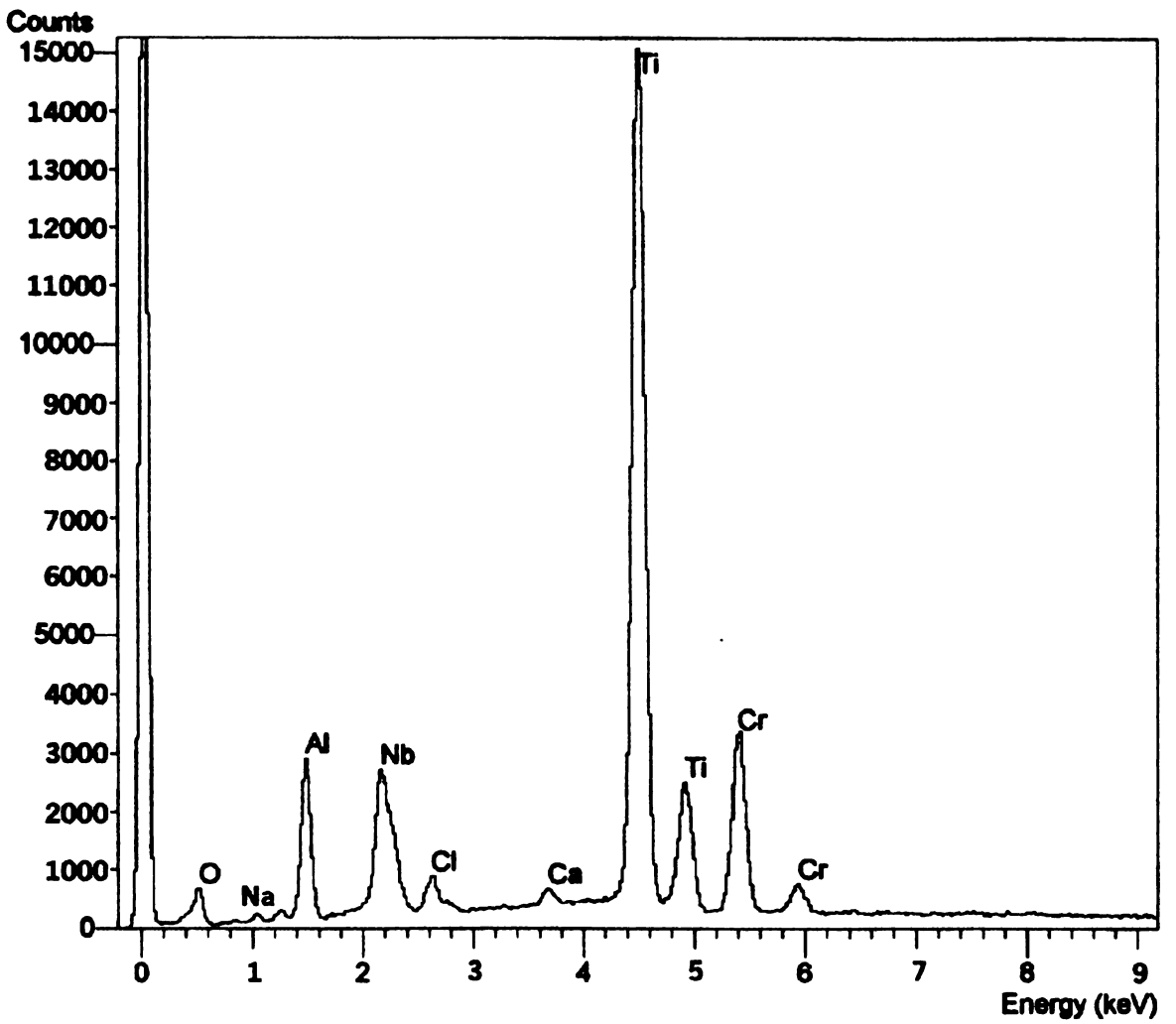

Figure 24. EDS scan of an attacked lamella region (α_2 phase) in Figure 23.

Nb, and about the same concentration of O. Figure 20 shows an oxide area where the salt deposition is light, area A, and other areas where the salt deposition was heavier, area B. The area where salt deposition is heavier is where the oxide growth is greater. Figure 21 shows the oxide scale that developed on the specimens exposed for 1.08 ks. The oxide has low concentrations of Al, Na and Cl.

Where the oxide layer is fractured in Figure 22, there is a decrease in Al concentration, and O, Na, and Cl was also detected. For the damaged region on the 1.08 ks specimens in Figure 23, there is a decrease in Al concentration, an increase in Nb and Cr concentrations; also O and Cl were detected. The EDS of the damaged region in Figure 23 is shown in Figure 24. The α_2 phase (Ti_3Al) is being preferentially attacked as evident from the erosion of lamallar microstructure. The 1.08ks specimens developed an oxide that spalled off, due to thermal shock, when the specimen was remove from the furnace, this did not occur on any of the other specimens.

Figure 25 shows the oxidized area on the specimen exposed for 19.44 ks. There are increased concentrations of Na, O, and a trace of Nb at the oxide surface. There was a decrease in Al concentration and no Cl or Cr at the oxide surface. At the interface of the oxide layer and metal, the Al concentration is lower. Figure 26 shows a damaged area, which was under the exfoliated oxide. The EDS scan (Figure 27) shows that the area has no concentration of Na or Cl, decreased Al concentration, and increased concentrations of Cr, Nb and O. Once again, the erosion of lamallar microstructure reveals α_2 attack. All the above EDS values are in comparison to the base metal.

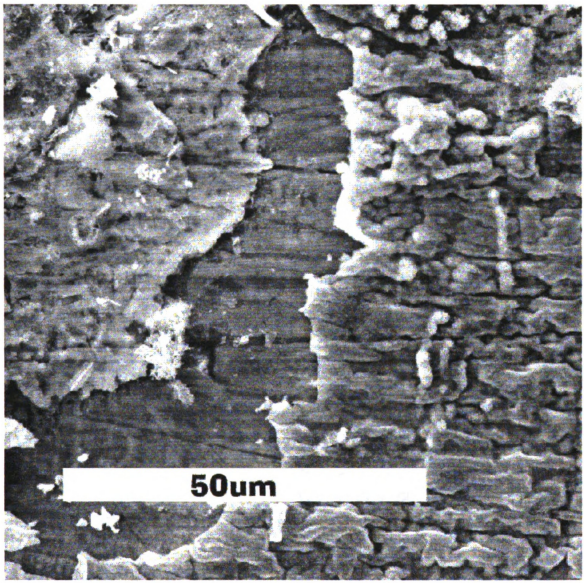

Figure 25. Specimen exposed for 19.44ks - exfoliated oxide.

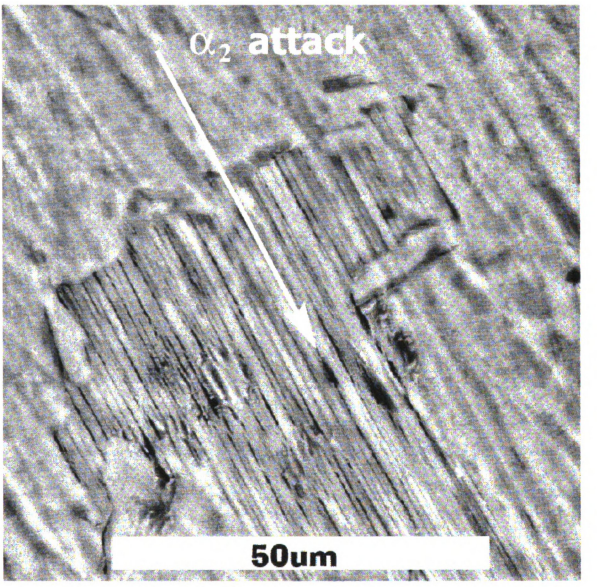

Figure 26 Specimen exposed for 19.44ks - damaged area under oxide.

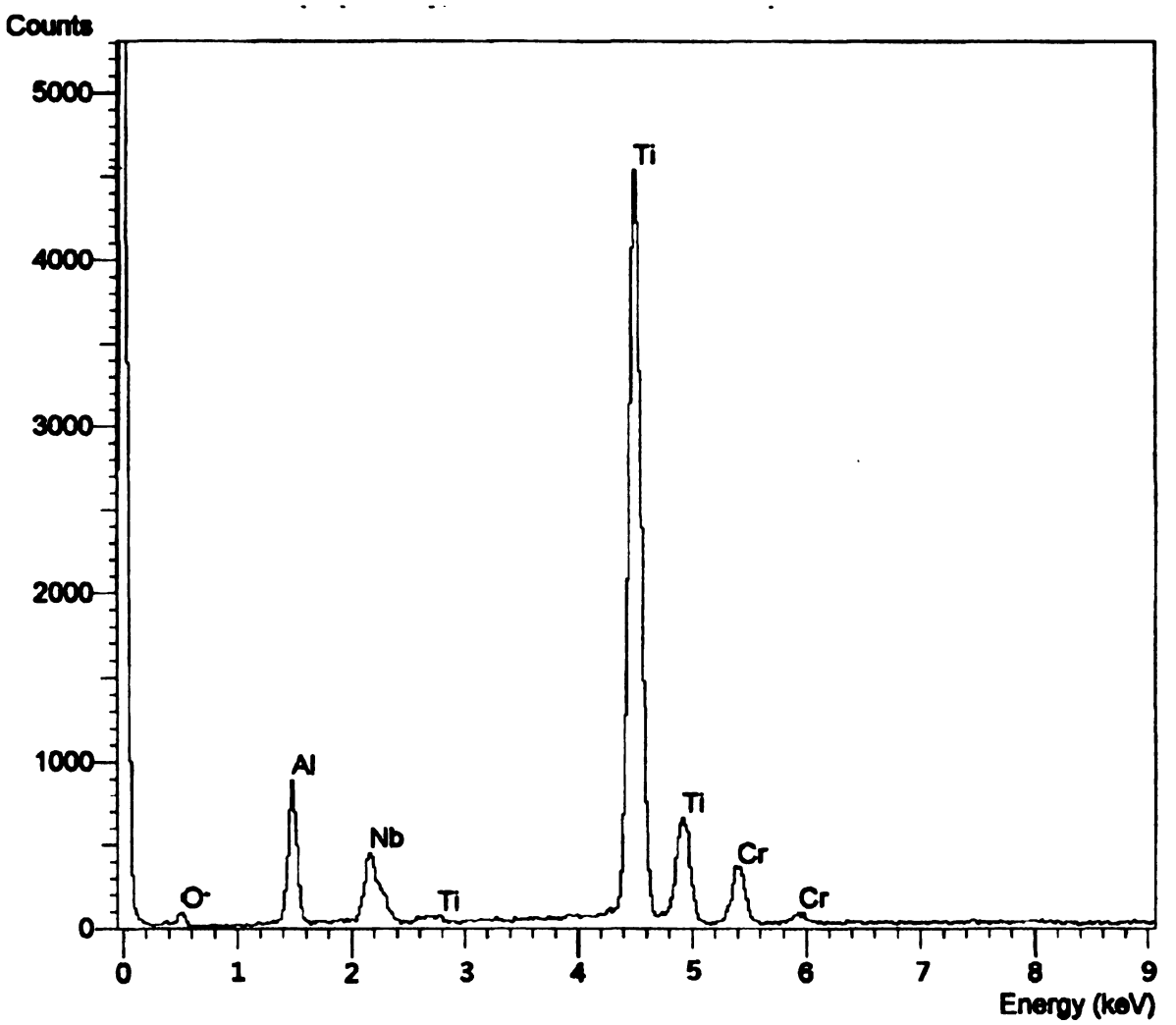

Figure 27. EDS scan of an attacked lamella region (α_2 phase) of Figure 25.

4.4 EFFECT OF SALT ATTACK ON FOUR-POINT BENDING STRENGTH

The four-point bend test results are given in Tables 3 for specimens that were exposed to salt and the elevated temperature cycle, and Table 4 gives results for specimens exposed to the elevated temperature cycle only. Figure 28 shows the plotted data for all specimens. From these results, it is apparent that a consistent degradation was observed for the longest time, whereas the fracture strength was variable and higher for the shorter exposures. This particular alloy has shown to have yield strengths close to 400 MPa which is comparable to 400 – 630 MPa yield strengths in the literature [3]. The variability in the fracture strengths may be attributed to uneven loading conditions, i.e., the test may have simulated a three point bend test in lieu of a four point bend test. This may be inferred due to the fact that most fractures occurred at or near the contact point between the upper pin and the specimen. Loading errors due to fixture slippage resulted in tests being restarted. Figure 29 shows the data for specimens that did not slip or fracture at a pin during the test, and shows a more accurate trend in decreasing strengths with increasing time. A schematic of the casting showing the locations from where the specimens were cut is shown in the inset of Figure 28.

Fracture initiation sites were sought in one specimen from each exposure time. There was little distinction that could be found between the specimens; all had multiple initiation sites along the tensile surface. Figure 30 Illustrates a region where the surface was not flat, possibly due to oxidation in a pitted area (arrow). However, most of the exposed surface near the fracture had no adherent oxide. Some residual oxide is evident at the arrow in Figure 31.

Table 3. Four-point bend results on specimens with salt application

Time ksec	MOR MPa	Length of pieces, mm	Comments on Fracture Location
0.15	480	25, 9	within 1 mm of pin, slight curvature in longer piece, fixture slipped-test restarted, top section of slab
0.15	410	21.5, 12.5	2.5 mm toward center from pin, fixture slipped-test restarted, top section of slab
0.15	516	8, 9.5, 16	at both pins
0.15	**469**		**AVERAGE VALUE**
0.36	474	21.5, 12.5	toward center, ≈2.5 mm from pin, fixture slipped-test restarted, top section of slab
0.36	616	23.5,10.5	at pin, fixture slipped-test restarted, top section of slab
0.36	444	26, 8	≈2 mm from pin
0.36	409*	23.3, 11.3	Fixture slipped twice before fracture within 1 mm of pin, *largest stress occurred on second loading, bottom section of slab
0.36	**486**		**AVERAGE VALUE**
1.08	571	25, 9	within 1 mm of pin, top section of slab
1.08	577	23, 11	within 1 mm of pin, top section of slab
1.08	142	25.5, 8.5	accidentally preloaded and bent, fractured ≈1.5 mm from pin, (not counted in avg.)
1.08	541	16.9, 17.9	Fracture near center of specimen, bottom section of slab
1.08	**563**		**AVERAGE VALUE**
4.4	492	11.3, 23.5	within 1 mm of pin, bottom section of slab
19.44	433	19.5, 14.5	in center, fixture slipped-test restarted, top section of slab
19.44	431	23, 11	within 1 mm of pin, fixture slipped-test restarted, top section of slab
19.44	423	24.5, 9.5	within 0.5 mm of pin
19.44	507	12.7, 22.1	within 2 mm of pin, bottom section of slab
19.44	**449**		**AVERAGE VALUE**

Table 4. Four-point bend results on specimens without salt application

Time ksec	MOR MPa	Length of Pieces, mm	Comments on test and fracture location
0.0	**523**(1) 480(2)		Ran test twice and could not fracture specimen due to repeated slipping of the fixture, bottom section of slab
0.36	565	24.18, 10.66	Fracture near inner pin, bottom section of slab
1.08	163(1) 111(2) **450**(3)	24.13, 10.64	Fracture near inner pin, fixture slipped twice before fracture accurring on third run, bottom section of slab
19.44	**529**	24.42, 10.33	Fracture near inner pin, bottom section of slab

Note: The number in parentheses shown in Table 4 refers to the loading run.

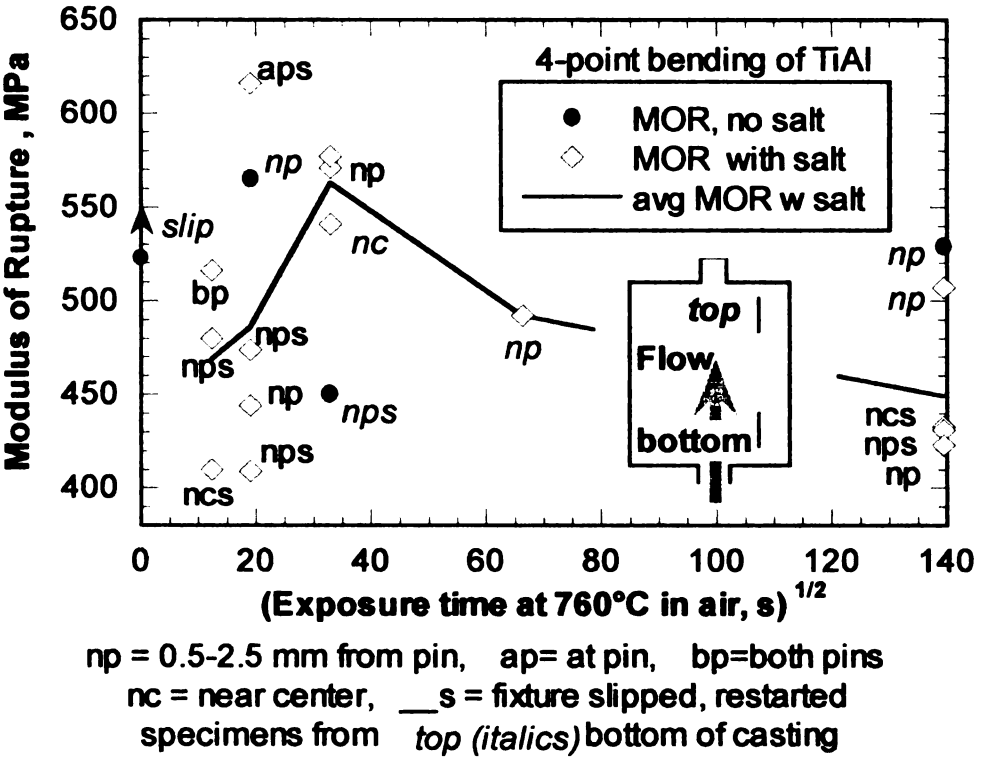

Figure 28. Effect of salt exposure on fracture strength

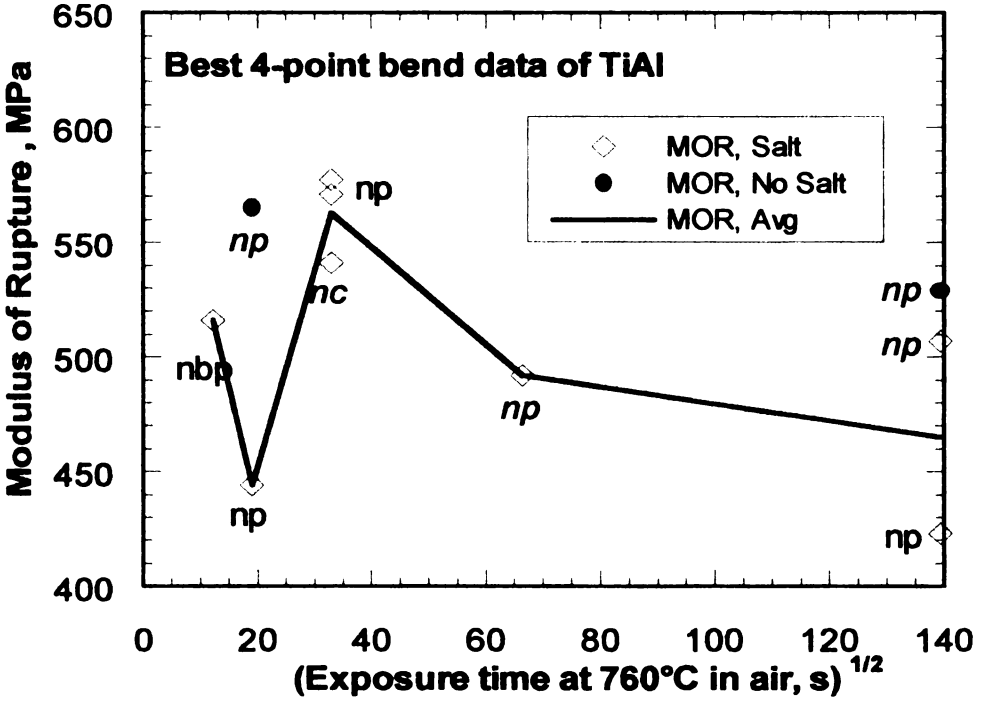

Figure 29. Fracture strength of specimens that had no slippage and not at a pin.

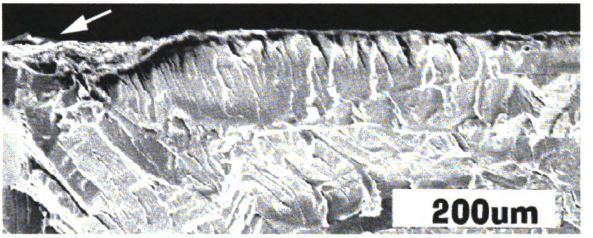

Figure 30. 0.36ks specimen fracture surface - oxidized pit.

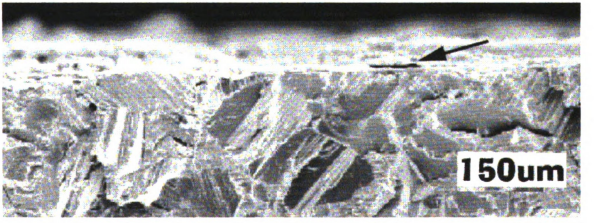

Figure 31. 19.44ks specimen fracture surface – remnant of spalled oxide.

4.5 SALT APPLICATION ON PRE-OXIDIZED SPECIMENS

The 3.6ks pre-oxidized specimens developed a discontinuous oxide layer. The oxide continued to grow after each cycle of salt and heat exposure and could be readily observed using light microscopy. Analysis by EDS revealed the presents of Na but no Cl, this trend continued for all cycles. The 3.6ks specimens developed surface morphologies similar to that shown in the upper right-hand corner of Figure 21. There were no obvious signs of salt attack unlike that which was observed on the bare specimens. Figures 32 and 33 show optical micrographs of the 3.6ks pre-oxidized specimens, the darker areas are oxide growth.

The 360ks pre-oxidized specimens developed a continuous oxide layer. The surface morphology of the oxide layer did not change after salt and heat cycling. There were particles observed on the oxide surface by ESEM, and the particles contained traces of Mg, Ca and Cl which are all constituents of the sea salt. Figure 34 depicts to general oxide covering on the 360ks pre-oxidized specimens, the particle shown on the surface of the oxide is a possible contaminant from the furnace.

4.5.1 Interrupted Weight Gain

Weight gain results for 3.6ks pre-oxidized specimens are shown in Figures 35. The slope is positive and reproducible for specimens that had salt applied and is zero for the specimen with no salt application. A photograph of the specimens after ten cycles is shown in Figure 36. It is obvious that NaCl stimulates oxide growth by the dark discoloration of the surfaces where the salt was applied in Figure 36.

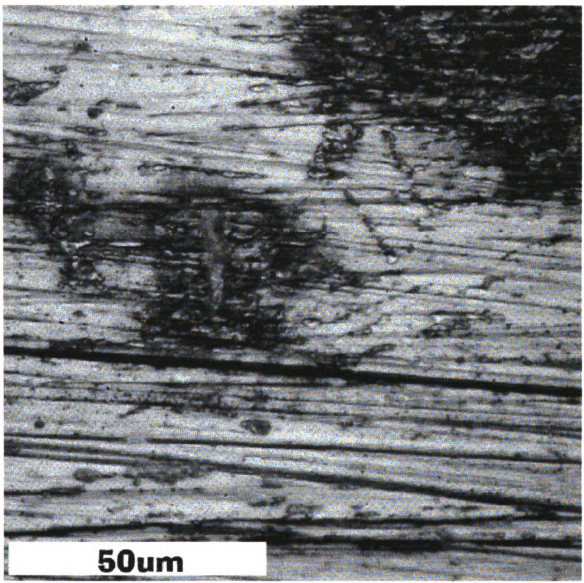

Figure 32. Pre-oxidation specimens after 1st Cycle - 3.6ks specimen

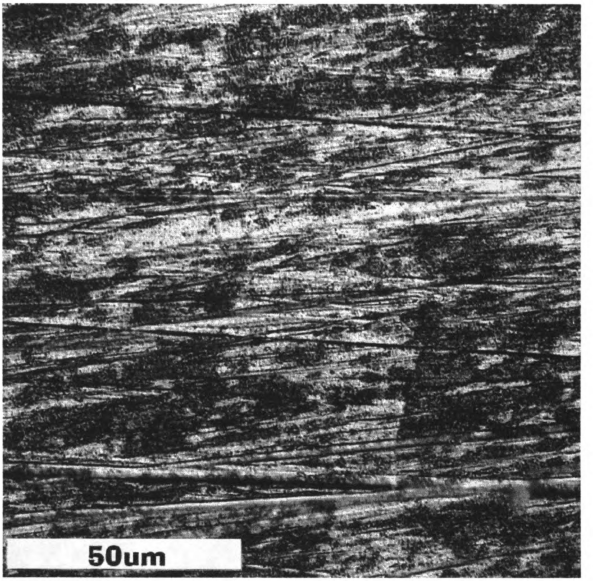

Figure 33. Pre-oxidation specimens after 10 Cycles - 3.6ks specimen.

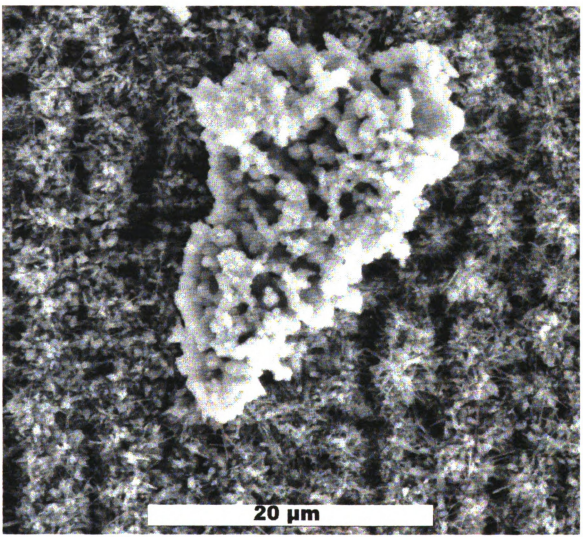

Figure 34. Pre-oxidation specimens after 1st Cycle - 360ks specimen

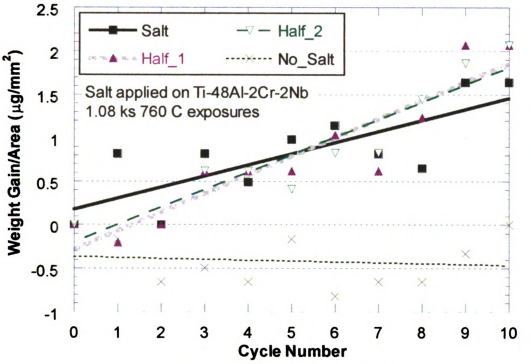

Figure 35. Plotted weight gain results.

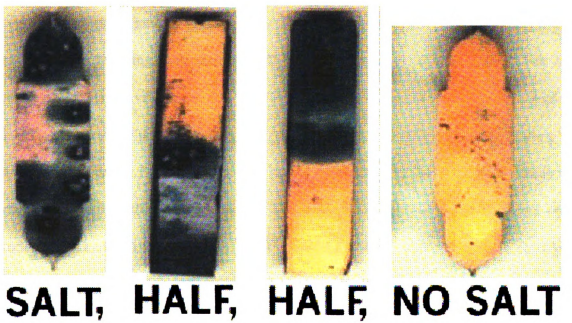

Figure 36. Weight gain photographs.

4.6 REACTIONS AND PRODUCTS

4.6.1 DTA

Differential thermal analysis of the casting filings and salt mixtures indicate that reactions occur at about 615 °C, 675 °C, 780 °C and 810 °C. These results are shown in Figure 37 where the reactions are labeled with an **R**. All the reactions are endothermic (DTA convention is that endothermic responses are indicated by the downward peak [54]) and start to occur at the label. The standard used was 99.999% pure Al, which has a melting point of 660 °C. The melting of the standard appears to be masked by reactions occurring in the mixtures. Similar results were obtained with the mechanically alloyed TiAl powder except that a reaction occurred at about 650 °C and between 720 °C to 730 °C as shown in Figure 38.

4.6.2 XRD

The x-ray diffraction performed on the 90wt% TiAl filings:10wt% salt identified many products resulting from the heating of the mixture during DTA. Table 5 lists all products that may have formed, the 1st through 4th 2θ angles are the diffraction angles identified by a peak finder program that match an element or compound. The plotted x-ray scan is shown in Figure 39 and the labeled peaks correspond with the numbers in brackets shown in Table 5. XRD on the 10wt% TiAl filings:90wt% salt identified two products, salt and γ-TiAl as shown in Table 6, and Figure 40 shows the plotted x-ray scan where salt is labeled S and γ-TiAl is labeled γ.

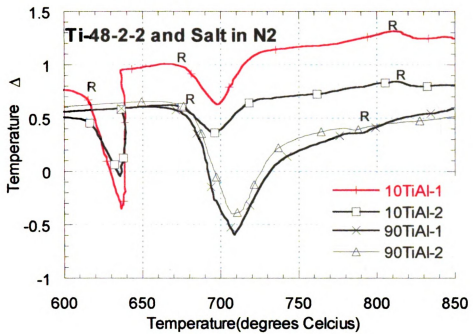

Figure 37. DTA of casting filings and salt.

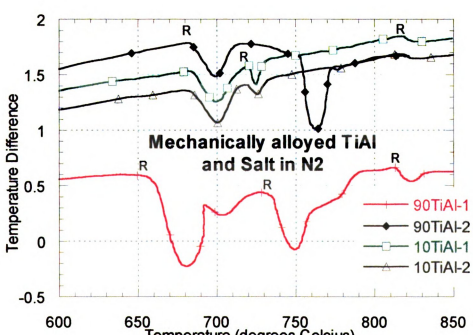

Figure 38. DTA of mechanically alloyed TiAl and salt

Table 5. Products identified by XRD on 90wt% TiAl filings:10wt% salt DTA powder

Species	strongest 2θ peak	2nd strongest 2θ peak	3rd strongest 2θ peak	4th strongest 2θ peak
TiO_2 (212)	27.474 [1]	36.170 [5]	54.257 [23]	68.973 [29]
Ti_xCr_yOOH (154)	27.474 [1]	36.290 [6]	35.847 [4]	
Ti_3Al (91)	54.257 [23]	41.264 [11]	72.182 [31]	
$Nb_{4.62}N_{2.14}$ (60)	36.170 [5]	38.743 [9]		
η-Cr_4Ti_4O (56)	41.264 [11]	43.452 [14]	42.261[12]	
$NbN_{0.6}O_{0.2}$ (52)	41.264 [11]	35.847 [4]		
$AlTi_3$ (51)	41.264 [11]	72.182 [31]		
Nb_2N (47)	35.847 [4]	33.845 [2]	38.410 [8]	
$NbTi_4$ (40)	54.748 [25]	39.127 [10]	42.261 [12]	
Cr (39)	39.127 [10]	44.253 [15]	48.53 [18]	
Na_2O_2 (36)	35.115 [3]	50.872 [21]		
TiAl (30)	38.743 [9]	45.581 [16]		
TiO (30)	43.152 [13]	43.452 [14]		

Note: The number in square brackets is the peak reference number in order of increasing 2θ and the number in parenthesis is the total intensity of all peaks identified for the species determined from the Scintag software peak finder (Figure 37).

Table 6. Products identified by XRD on 90wt% TiAl filings:10wt% salt DTA powder

Species	strongest 2θ peak	2nd strongest 2θ peak	3rd strongest 2θ peak	4th strongest 2θ peak
TiAl	21.20	45.68	65.72	
NaCl	31.689	45.448	56.523	27.374

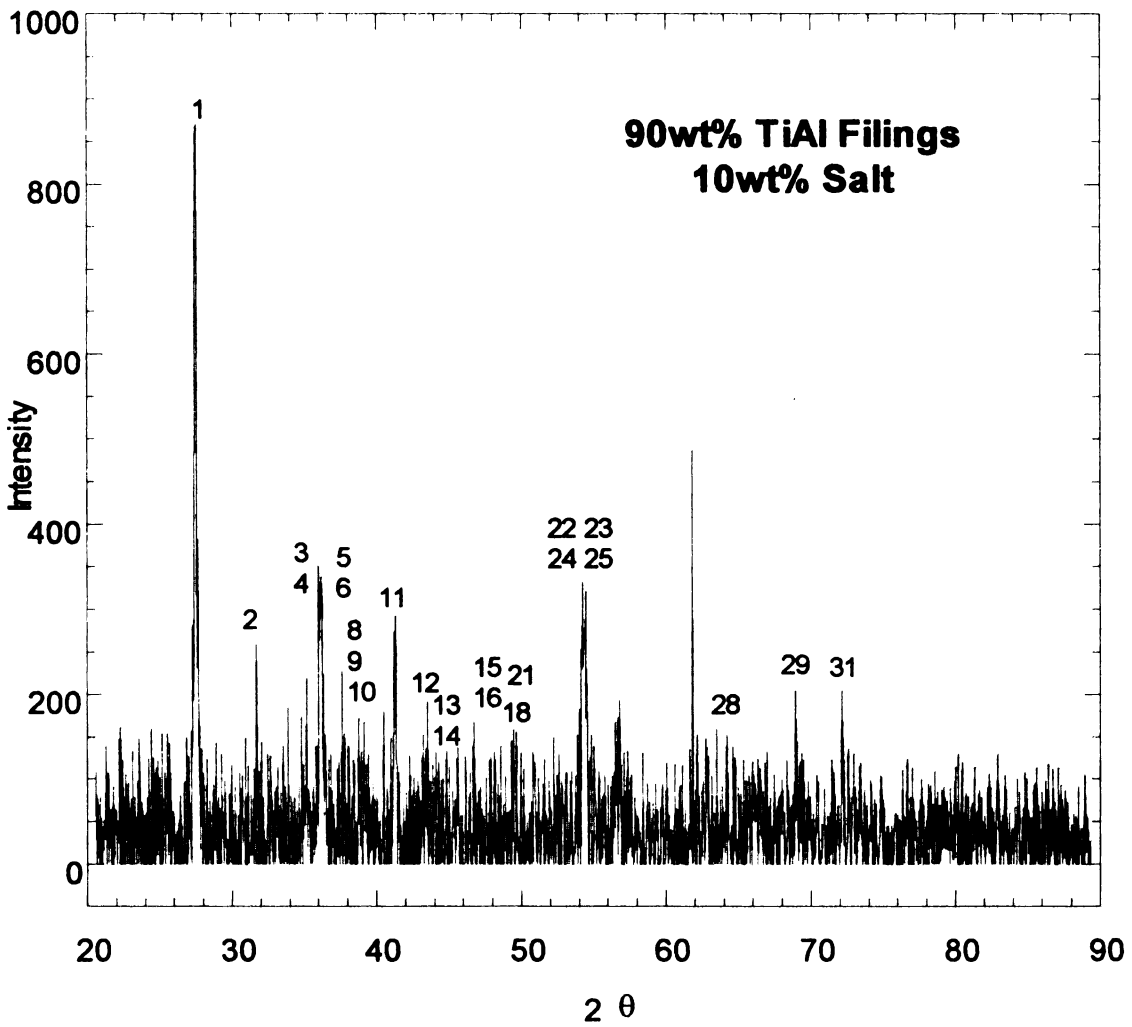

Figure 39. XRD scan of 90wt% TiAl filings:10wt% salt DTA powder.

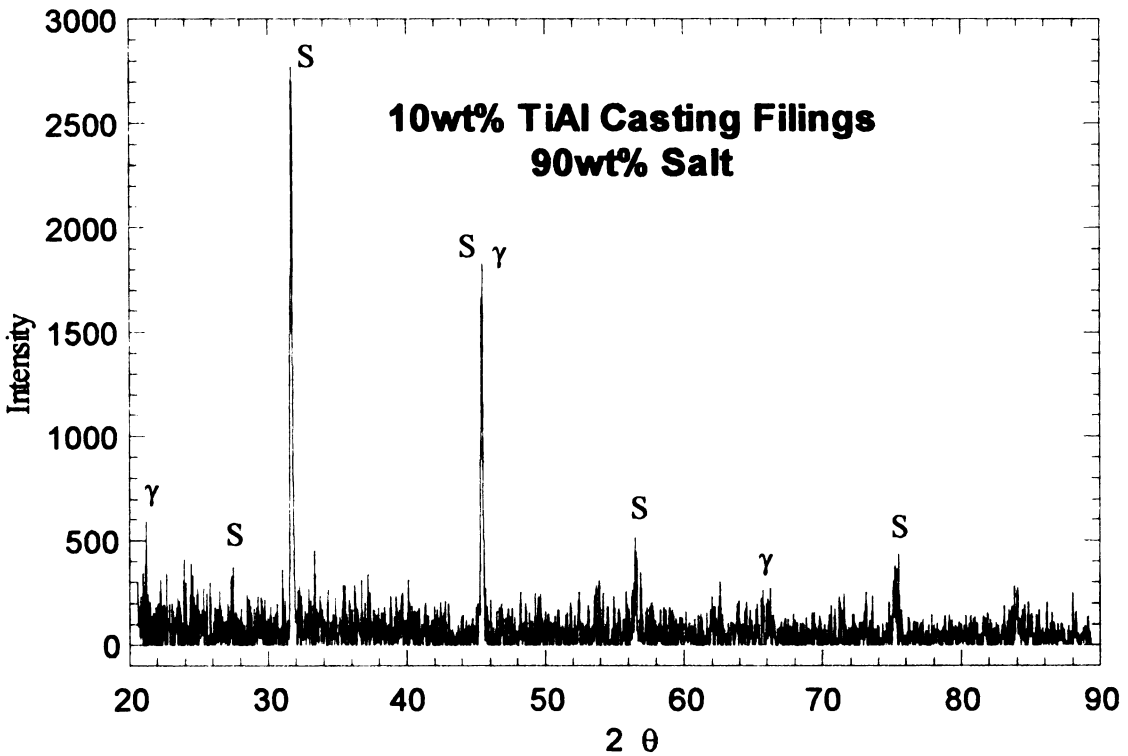

Figure 40. XRD scan of 90wt% TiAl filings:10wt% salt DTA powder.

CHAPTER 5

ANALYSIS AND DISCUSSION

5.1 INTRODUCTION

Reactions between the alloy, Ti-48Al-2Cr-2Nb, and NaCl, when exposed to high temperatures, appear to be detrimental to the alloy by preferential attack of the α_2 phase if it is not pre-oxidized. It is apparent that the reaction kinetics between the bare metal and NaCl occur at a much greater rate than the reaction kinetics between the alloy's natural oxide and NaCl.

Two forms of oxidation were observed, a smooth surfaced and dense form that increased in thickness with time, and heterogeneous eruption of needle and plate shaped crystals the grew quickly from a point on the smooth oxide surface. The presence of salt appeared to stimulate the growth of the latter type, which is evident in Figures 20 and 32, and is clearly not a protective oxide. From ref. [16], the latter type of oxide is fast growth of TiO_2. At temperatures greater that 700°C, growth of TiO_2 is faster than Al_2O_3. At 900°C in an air, an alloy with activities of 1 for Ti and Al, Al_2O_3 is slightly more stable than TiO_2. Changes in activities to either species due to the introduction of another species (i.e., Cr, Nb, etc.) can alter this stability. However, in experiments, Al_2O_3 formation is often observed to occur in the beginning of the oxidation process, leading to depletion in Al and a Ti enrichment [16]. This may account for the low EDS values for aluminum, where the concentration is low at the metal and oxide surfaces as seen in Figure 9a.

5.2 ELEMENTAL TRENDS

EDS measurements were used to determine elemental trends. Each EDS scan was standardized to the total titanium counts detected during that scan. There were high concentrations of Na detected on the oxide surface, and low concentrations at metal surfaces and interfaces (Figure 8a). The surface Na concentration increased with time. The vapor pressure of sodium at 760°C is about 230 torr. (0.3 atm.), so Na evaporation is possible. Sodium ions are known to transport through alumina, and the sodium may also react with alumina to form Na_xAlO_y [15]. Exposure to NaCl at 760 °C may lead to the formation of Na_5AlO_4, in a manner similar to the equations in the introduction. However, x-ray diffraction experiments indicate the presence of Na_2O_2 (Figure 37 and Table 5) that was formed by a reaction(s) between Na and oxides that were present on the casting. The probability of Na_2O_2 formation is low, because there are only two characteristic peaks of low intensity and the low availability of oxygen. There is a higher probability that TiO_2 forms since it is the more stable oxide. The availability of oxygen in the system is limited because the DTA powder used was heated in a nitrogen atmosphere (100ml per minute purge was used). Oxygen may have come from either previous formed oxides on the casting surface or interstitial oxygen.

Chlorine concentrations are high in and around pitted areas, and surrounding oxides, especially at early times (the 0.15 and 0.36ks specimens in Figure 8b). Chlorine ions can act as a catalyst for oxide growth on bare metal specimens [16] since chlorine tends to stay on the metal surface until sufficient oxide has developed. At longer exposure times the Cl concentrations decrease toward zero at the surface (Figure 8a) and increases at the interfaces and oxide layers. This could happen due to the higher vapor pressure of Cl that

allows it to escape, or a dilution effect as the oxide grows. X-ray diffraction analysis of the 10wt% salt:90wt% TiAl powder mixture detected no chlorine containing compounds present, the only chlorine containing compound detected in the 90wt% salt:10wt% TiAl powder mixture was NaCl.

The oxygen concentration increases as exposure time increases (Figure 9b), which is expected since titanium and aluminum oxides layers grow thicker with time. The observed relative decrease in aluminum concentrations at the oxide surface is consistent since TiO_2 is known to grow faster and occupy the outer oxide layer [10]. However, the decreased aluminum concentration at the metal interface implies that either aluminum atoms evaporate, or that alumina forms in locations that are not as easily detected by EDS (e.g. in the oxide close to the metal surface, [10]

There are higher concentrations of Cr and Nb at and around damaged or pitted areas (Figure 10), where much greater amounts of Ti and Al were consumed to form oxides. Nb is added to TiAl alloys to enhance their oxidation resistance by formation of Nb_2O_5 within the $TiO_2/Al_2O_3/Nb_2O_5$ oxide layer [37]. The exposure to salt precluded the formation of Nb_2O_5 oxide, but salt may have catalyzed the formation of $NbTi_4$, Nb_2N and NbN_xO_y (Table 5). Cr additions are detrimental to oxidation resistance and are only added to improve ductility. The exposure to hot corrosion by NaCl may have decreased the ductility due to the formation of Cr_4Ti_4O (Table 5).

Nitrogen was not detected in any of the EDS scans. Rakowski detected TiN in the oxide interfacial region of specimens exposed at 800 – 900 °C in air and atmospheres containing various amounts of nitrogen [31], where the presence of TiN interferes with the formation of a protective oxide layer. The volume fraction of TiN was not reported,

so if it is small, it may not be detectable. This alloy will form TiN within its oxide layers after long time exposure (9000 hours) at 704 °C in air [33]. XRD detected nitrogen compounds (Table 5) where the nitrogen reacted with niobium in lieu of titanium.

5.3 STRENGTH OF EXPOSED SPECIMENS

There is no significant effect of accelerated oxidation on the fracture strength due to salt and heat exposure for short times on bare ground specimens. The presence of multiple initiation sites indicates that flaws due to local attack were below the critical crack length. The variability in the fracture strengths may be attributed to variations in local orientation conditions in regions of maximum stress and/or imperfect loading conditions. Only the longest exposure time showed a decrease in the scatter in strength, but these fracture strengths were still above the yield stress [3] and above the lowest values obtained in specimens with short or no exposure (Table 3, Table 4 and Figure 27).

The variation in strength of the specimens can also be correlated to imperfections in the loading conditions or specimen dimensions. Imperfect loading led to conditions more similar to a three-point bend test than a four-point bend test. The three-point bend test condition may be inferred due to the fact that the specimens with the highest strength fractured at or near the contact point between the upper pins and the specimen. During this test condition a smaller volume of material was subjected to the maximum stress, and the probability of a flaw or a microstructural condition that stimulates fracture initiation is lower. The lower fracture strengths correlate with fracture positions farther from the pin locations, this is typical for the four point bend test condition where a larger volume of material was subjected to a more uniform stress state. During this test condition the probability of a flaw or a microstructural condition that stimulates fracture initiation is

higher which implies that damage due to salt attack did not create surface damage severe enough to become critical in the regions between the pins.

The lack of the oxide on the fracture surfaces may be attributed to either the effect of salt in making the oxide non-adherent, or spallation due to the release of strain energy during fracture. Also, there is a thermal expansion mismatch between the oxide and alloy that could promote de-bonding at the interface. The oxide may have spalled off or de-bonded prior to fracture (as in the case of the 1.08ks specimens). The oxide that developed on specimens exposed to salt appears to enhance the strength up to exposure times of 1.08ks, but thermal shock may have caused the oxide to spall in the conditions of this experiment (Figure 29), so thermal shock may degrade the oxide strength with longer exposure times. An investigation using slower cooling rates is necessary to evaluate whether the degraded strength is due to thermal shock or the nature of the accelerated oxide growth.

It is apparent that pitting and preferential attack of α_2 occurs on bare ground surfaces of the alloy during short exposure times in the presence of salt, but this damage is not severe. However, the oxides stimulated by salt are not adherent. Since the oxides layers that form during hot corrosion by NaCl are non-protective (i.e., not continuous), there is a possibility for hydrogen embrittlement or oxygen absorption (α-case embrittlement) to occur and degrade the alloys strength [1, 34, 42]. It is not clear whether the non-adherent oxides will fall off in engine conditions, taking the salt with it and subsequently allowing a more protective oxide to develop before further exposure to salt occurs.

5.4 EFFECTS OF PRE-OXIDATION

Pre-oxidizing is beneficial to limit or prevent surface damage caused by hot corrosion by NaCl on this alloy. Pre-oxidation prevented spalling upon removal from the furnace, and the surface oxides were not easily removed with a pick. The presence of sodium but not chlorine in EDS measurements suggests that the Cl evaporates. Short pre-oxidation times result in a discontinuous oxide consisting of thin, if not transparent oxide, and regions where platelets of TiO_2 emanate from a point region to form a porous oxide on the surface. With increasing time these more porous oxide features cover a larger fraction of the specimen.

Weight gain by this oxidation mechanism is accelerated with the application of salt, as shown in Figures 33 and 34. These results agree with similar weight gain results obtained by Yao and Marek [15] on a Ti-47Al-2Nb-2Mn + 7vol% TiB_2 alloy that had NaCl-induced hot corrosion. Their study shows that salt increases the slope of initial oxidation kinetics. After an incubation period the oxidation kinetics of the salt exposed specimens switch from linear to parabolic similar to other TiAl alloys which have not been exposed to salt [10, 16, 31, 33, 37]. Thus salt apparently stimulates formation of rapid growing titanium oxide evident in the periphery of Figure 32. For the longer pre-oxidation time of 360ks, NaCl has no obvious effect on the oxide layer, which had the fast growing porous TiO_2 oxide layer on the surface. It is clear from these experiments that salt stimulates the formation of these porous oxides that cause rapid weight gain from a pre-existing smooth and dense oxide. However, such oxides also form on specimens that have no salt exposure.

The direct application of salt to bare TiAl alloys causes growth of a non-protective scale, but it is not known whether the application of salt on an oxidized surface will degrade a protective layer. Thus, further study is needed to quantify the effect that salt has on the growth rate of the porous oxide on an existing oxidized surface, and the relationship that this rapid growth has on the metal/oxide interface.

CHAPTER 6

CONCLUSIONS AND RECOMMENDATIONS

6.1 CONCLUSIONS

A method to apply salt water to specimens that is similar to natural conditions near sea coasts was developed and used to apply salt to bare ground and pre-oxidized specimens of Ti-47.9Al-2Cr-2Nb alloy. After exposure in a 760°C air furnace for times between 0.15 - 20 ks, the salt stimulated rapid growth of non-protective porous oxides on specimens with bare ground surfaces. Pitting that attacked the α_2 (Ti_3Al) phase preferentially was evident in regions where the non-protective oxide was spalled off. However, such pits had no apparent effect on fracture initiation in 4-point bending.

Pre-oxidizing the surface prevented the spalling of the oxide observed in the bare ground specimens. From EDS measurements, Cl was most often found in the metal-oxide interface when salt was directly applied to bare ground specimens, and Na was most often found on the surface of the oxide on both the bare ground and pre-oxidized specimens.

6.2 RECOMMENDATIONS FOR FUTURE RESEARCH

Further investigations are needed to determine if a non-adherent oxide will fall off in engine operating conditions, taking the salt ions with it, and if a protective and adherent oxide will grow in its place. Also, the longer term effects of accelerated oxide growth due to salt need to be examined to determine whether condensation of water containing sea salt will have any detrimental effect on the long term stability of protective oxides.

The oxide layer that forms during hot corrosion consists of many different products. These products might form at different areas within the oxide layer. Exposure time might

influence the location of the products within the oxide layer. Results from this study indicate that fracture strength (modulus of rupture) reaches maximum values at about 1.08ks (18 min.), and that reaction products between salt and the alloy could reside within the oxide layer (Table 5). Previous oxidation studies (performed in air or O_2) on titanium aluminides [31, 33, 37] have identified Nb_2O_5 and TiN as reaction products present in the oxide layers. It would be beneficial to determine if there is a correlation between the reaction products, their location in the oxide layer, and fracture strength. X-ray photoelectron spectroscopy (XPS) may be utilized to perform this identification process by examining a cross-section of the oxide layer, and determining if bonding within the oxide changes with exposure time and position.

Another research path that might elucidate strength degradation caused by hot corrosion is to perform *in-situ* testing of a stressed sample within an ESEM that provides an atmosphere of appropriate gases. Advantages to performing this type of testing are: the growth kinetics of the oxide can be viewed and recorded; its possible to determine a rupture stress at exposure temperatures; to see how surface damage could affect elevated temperature deformation phenomena such as creep crack growth, by monitoring stress relaxation or strain with constant loading conditions. A main disadvantage is the difficulty controlling the temperature of the specimen without causing too much localized heating or burning out the heating device. Such i*n-situ* testing was attempted but problems were encountered with heater controller and the integrity of the heating element. The limited space within the tensile test fixture of the ESEM and the size of the specimens presents a challenge to designing the heating device.

An investigation using slower cooling rates could determine if there is a correlation between fracture strength and thermal shock or the nature of the oxide growth. Also, longer cyclic studies on specimens with thicker pre-oxidation oxide layers can elucidate if thicker oxides are more protective, this will be evident if thicker pre-oxidation layers gain less weight than thinner pre-oxidation layers. Longer cyclic studies will determine the rate kinetics of accelerated oxidation, i.e., if the behavior turns parabolic, cubic or continues to be linear. The alloy studied by Yao and Marek [15] switched from a linear behavior to a parabolic behavior similar to other TiAl alloys which had no salt exposure [10, 16, 31, 33, 37].

A very important aspect when studying hot corrosion is to simulate, as closely as possible, conditions within an engine. Burner rigs can accomplish this but they are not simple or economic, especially in an academic setting. A proposed way of simulating engine conditions is heating an exposed specimen within an alumina vessel, while controlling a flow of engine gases through the vessel. The main problem with this approach is handling the engine gases, which can be toxic.

BIBLIOGRAPHY

1. Kim, Y-W. and Froes, F.H. "Physical Metallurgy of Titanium Aluminides." *High Temperature Aluminides and Intermetallics.* The Minerals, Metals & Materials Society (1990): 465-492.

2 Lipsitt, H.A., Shechtman, D. and Schafrik, R.E. "The Deformation and Fracture of Ti_3Al at Elevated Temperatures." *Metallurgical Transactions A.* 11A (1980): 1369-1375.

3. Kim, Y-W. "Intermetallic Alloys Based on Gamma Titanium Aluminide." *JOM.* July (1989): 24-30.

4. Kim, Y-W and Dimiduk, D.M. "Progress in the Understanding of Gamma Titanium Aluminides." *JOM.* August (1991): 40-47.

5. Austin, C.M. and Kelly, T.J. "Development and Implementation Status of Cast Gamma Titanium Aluminide." *Structural Intermetallics.* The Minerals, Metals & Materials Society (1993): 143-150.

6. Larsen, J.M., Williams, K.A., Balsone, S.J. and Stucks, M.A. "Titanium Aluminides For Aerospace Applications." *High Temperature Aluminides and Intermetallics.* The Minerals, Metals & Materials Society (1990): 521-555.

7. Nishiyama, Y., Niyashita, T., Susumu, I. and Noda, T. "Development of Titanium Aluminide Turbocharger Rotors." *High Temperature Aluminides and Intermetallics.* The Minerals, Metals & Materials Society (1990): 557-584.

8. Yamaguchi, M. "High Temperature Intermetallics – With Particular Emphasis on TiAl." *Materials Science and Technology.* Vol. 8 April (1992): 299-307.

9. Misra, A.K. "Reaction of Ti and Ti-Al Alloys With Alumina." *Metallurgical Transactions A.* 22A (1991): 715-721.

10. Taniguchi, S. and Shibata, T.. "Influence of Additional Elements on the Oxidation Behavior of TiAl." *Intermetallics.* 4 (1996): S85-S93.

11. Rapp, R.A., "Chemistry and Electrochemistry of the Hot Corrosion of Metals.", *Corrosion.* Vol. 42 No. 10 (1986): 568-577.

12. *Failure Analysis and Prevention*,4th ed., ASM International, Metals Park, Ohio, 1992, pp. 280.

13. ASM. *Metals Handbook Desk Edition.* 7th ed., Metals Park, Ohio:ASM International, pp. 9•10, 1992.

14. ASM. *Metals Handbook Desk Edition..* 7th ed., Metals Park, Ohio:ASM International, pp. 1•33, 1992.

15. Yao, Z. and Marek, M., "NaCl-Induced Hot Corrosion of a Titanium Aluminide Alloy." *Mater. Sci. & Eng.* **A192/193** (1995): 994-1000.

16. Schutze, M. and Hald, M., "Improvement of the Oxidation Resistance of TiAl Alloys by Using The Chlorine Effect." Materials Division, Karl-Winnacker-Institut der DECHEMA e. V., D-60061 Frankfurt am Main.

17. S. Taniguchi, *Materials and Corrosion* 48 (1997): 1-9.

18. Liu, C.T., "Recent Advances in Ordered Intermetallics." Materials Research Society Symposium Proceedings, Vol 288 (1993): 3-19.

19. ASM. *Alloy Phase Diagrams.* ASM Handbook Vol. 3., Metals Park, Ohio:ASM International, pp. 2•54, 1992.

20. Wright, P.K., "On Ductility and Toughness Requirements for Intermetallics in Aircraft Engines." *Structural Intermetallics*, Materials Research Society (1993): 885–893.

21. Yamaguchi, M. and Inui, H., "TiAl Compounds For Structural Applications." *Structural Intermetallics*, Materials Research Society (1993): 127–142.

22. Seo, D.Y., Bieler, T.R., An, S.U. and Larson, D.E., "Changes in Microstructure During Primary Creep of a Ti-47Al-2Nb-1Mn-0.5W-0.5Mo-0.2Si Alloy." *Metallurgical Transactions A.* 29A (1998): 89-98.

23. Fontana, M.G. *Corrosion Engineering.* New York: McGraw-Hill, 1986.

24. Moretti, G., Quartarone, G., Tassan, A. and Zingales, A., "Pitting Corrosion Behavior of Superferritic Stainless Steel in Waters Containing Chloride." *Werkstoffe and Korrosion.* 44 (1993): 24-30.

25. Gregory, J.K. and Brokmeier, H.G., "The Relationship Between Crystallographic Texture and Salt Water cracking Susceptibility in Ti-6Al-4V." *Mater. Sci. & Eng.* **A203** (1995): 365-372.

26. Ricker, R.E., Hall, D.E. and Fink, J.L., "The Effect of Aqueous Environements on the Fracture Behavior of Ductile Nickel Aluminide." *Scr. Metall. Mater.* 24 (1990) 291-296.

27. Bavarian, B., Hartutouni, S. and Zamanzadeh, M., "Evaluation of the Environmentally assisted Cracking of Aluminide Intermetallic Compounds." *Mater. Sci. & Eng.* **A153** (1992): 613-618.

28. Ricker, R.E., "Origins of the Aqueous Corrosion and Stress Corrosion Cracking Behavior of Ductile Nickel Aluminide." *Mater. Sci. & Eng.* **A198** (1995): 231-238.

29. Meier, G.H., Pettit, F.S., and Hu, S., "Oxidation Behavior of Titanium Aluminides." *J. De Physique IV*, Colloque **C9** (1993): 395.

30. Cole, I.S. And Ganther, W., "A Preliminary Investigation into Airborne Salinity Adjacent to and Within the Envelope of Australian Houses", Construction and Building Materials Vol. **10** No. 3 (1996): 203-207.

31. Rakowski, J.M., Pettit, F.S., Meier, G.H., Dettenwanger, F., Schumann, E., Ruhle, M., "The Effect of Nitrogen on the Oxidation of γ-TiAl." *Scripta Metall.* Vol. **33** No. 6, (1995): 997-1003.

32. Rahmel, A. and Spencer, P.J., "Thermodynamic Aspects of TiAl and $TiSi_2$ Oxidation: The Al-Ti-O and Si-Ti-O Phase Diagrams." *Oxidation of Metals* Vol. 15 No. 1/2, (1991): 53–68.

33. Brady, M.P., Brindley, W.J., Smialek, J.L. and Locci, I.E., "The Oxidation and Protection of Gamma Titanium Aluminides." *JOM.* August (1996): 46-50.

34. Du, H.L., Datta, P.K., Lewis, D.B. and Burnell-Gray, J.S., "Air Oxidation Behaviour of Ti-6Al-4V Alloy Between 650°C and 850°C." *Corrosion Science* Vol. 36 No. 4, (1994): 631-642

35. CRC. *Handbook of Chemistry and Physics.* 79th ed., Boca Raton, FL:CRC Press Inc., 1998.

36. Tsuyama, S., Mitao, S. and Minakawa, K., "Alloy Modification of γ-Base Titanium Aluminides for Improved Oxidation Resistance, Creep Strength and Fracture Toughness." *Mater. Sci. & Eng.* **A153** (1992): 451-456.

37. Kim, B.G., Kim, G.M. and Kim, C.J., "Oxidation Behavior of TiAl-X (X=Cr, V, Si, Mo, Nb) Intermetallics at Elevated Temperatures." *Scripta Metall.* Vol. **33** No. 7, (1995): 1117-1125.

38. Partridge, A. and Winstone, M.R., "Oxidation Behavior of Highly Alloyed γ-TiAl Alloys." *Structural Intermetallics*, Materials Research Society (1997): 405–410.

39. Streiff, R. and Poize, S., "Oxidation of Aluminide Coatings on Unalloyed Titanium." *High Temperature Corrosion*, ed. Rapp, R.A. Houston, TX: NACE (1983): 591–597.

40. Zhang, Y.G., Li, X.Y., Chen, C.Q., Zhang, X.J., Zhang, T.H. and Zhang, H.X. "The Influence of Ion Implantation Upon High Temperature Oxidation Behavior of Ti-48at.%Al Alloy." *Structural Intermetallics*, Materials Research Society (1997): 353-360.

41. Kawaura, H., Nishino, K. and Saito, T., "New Surface Treatment Using a Fluidized Bed Furnace For Improving Oxidation Resistance Of TiAl-Based Alloys." *Structural Intermetallics*, Materials Research Society (1997): 377–383.

42. McKee, D.W. and Huang, S.C., The Oxidation Behavior of Gamma-Titanium Aluminide Alloys Under Thermal Cycling Conditions." *Corrosion Science*, Vol. 33 No. 12 (1992): 1899-1914.

43. Rapp, R. A. and Zhang, Y.S., "Hot Corrosion of Materials: Fundamental Studies." *JOM.* August (1994): 47-55.

44. Bornstein, N.S. and DeCrescente, M.A., "The Role Of Sodium and Sulfur in the Accelerated Oxidation Phenomena – Sulfidation." *Corrosion*, Vol. 26, No. 7 (1970): 209-214.

45. Goebel, J.A., Pettit, F.S. and Goward, G.W., "Mechanisms for the Hot Corrosion of Nickel-Base Alloys." *Metallurgical Transactions*, Vol. 4 (1973): 261–278.

46. Deb, D., Ramakrishna Iyer, S. and Radhakrishnan, V.M., "Assessment of High Temperature Performance of a Cast Nickel Base Superalloy in Corrosive Environment." *Scripta Materialia*, Vol. 35 No. 8 (1996): 947–952.

47. Gaskel, D.R., *Introduction to Metallurgical Thermodynamics.* 2nd ed. New York: Hemisphere Publishing Corporation, 1981.

48. Hiramatsu, N., Uematsu, Y., Tanaka, T. and Kinugasa, M., "Effect of Alloying Elements On NaCl-Induced Hot Corrosion of Stainless Steels." *Mater. Sci. & Eng.* **A120** (1989): 319-328.

49. Fujikawa, H. and Maruyama, N., "Corrosion Behavior of Austenitic Stainless Steels in the High Chloride-Containing Environment." *Mater. Sci. & Eng.* **A120** (1989): 301-306.

50. Saunders, S.R.J. and Nicholis, J.R., "Hot-Salt Corrosion Testing – An International Intercomparison." *Materials at High Temperatures*, Vol. 13, No. 3 (1995): 115–120.

51. Chaze, A.M. and Coddet, C., "Influence of Aluminum on The Oxidation Of Titanium Between 550 and 750 °C." *Journal of the Least Common Metals*, 157 (1990): 55–70.

52. Du, H.L., Datta, H.L., and Hwang, S.K., "High Temperature Corrosion Behavior of Ti-46.6Al-1.4Mn-2Mo in Environments of Low Oxygen and High Sulfur Potentials at 700 °C and 900 °C." *Materials Science Forum*, Vol. 251-254 (1997): 219–226.

53. Saitoh, Y., Asakawa, K. and Mino, K., "Embrittlement of Titanium Aluminides By Slight Oxidation." *Aspects of High Temperature Deformation and Fracture in Crystalline Materials* Proceedings of the 7th JIM International Symposium (1994): 583–589.

54. Brown, Michael E., *Introduction to Thermal Analysis Techniques and Applications.* New York:Chapman and Hill, 1988.